



Original research article



Sequence extraction-based low voltage ride-through control of grid-connected renewable energy systems

Fayçal Benyamina^{a,b}, Hafiz Ahmed^c, Abdeldjabar Benrabah^a, Farid Khoucha^{a,b}, Yahia Achour^a, Mohamed Benbouzid^{b,d,*}

^a Ecole Militaire Polytechnique, UER ELT, 16111 Algiers, Algeria

^b University of Brest, UMR CNRS 6027 IRDL, 29238 Brest, France

^c Nuclear AMRC, University of Sheffield, Derby DE73 5SS, UK

^d Shanghai Maritime University, Shanghai, China

ARTICLE INFO

Keywords:

Grid-connected converters

Low voltage ride-through

Grid codes

Sequence extraction

Grid-synchronization

Adaptive observers

ABSTRACT

Various faults can cause voltage sag in the power grid at different voltage levels across the network. Balanced or unbalanced voltage sags lead to grid instability by tripping off a large number of wind or solar power plants from the electric power network. This is particularly problematic to maintain the stability of renewable energy-rich converter-dominated modern power systems. To mitigate the adverse effects of voltage sag, grid-connected converters (GCCs) need to be capable of operating in self-healing and fault-tolerant mode by embedding low voltage ride-through (LVRT) capability into the control system of GCCs. In order to facilitate the implementation of LVRT capabilities for unbalanced faults, fast and accurate frequency-adaptive sequence extraction of grid voltages and currents is essential. This motivated the present work of making a systematic comparison of adaptive observer-based sequence extraction techniques to provide LVRT capabilities into the control system of GCCs. In order to show the effectiveness of each observer, various comparative analyses were performed through Matlab-based numerical simulation. Different observers were benchmarked by the dynamic performance improvement during the low-voltage fault period. Experimental results using a laboratory-scale prototype GCC show that adaptive observers are a suitable choice of sequence extractors for LVRT operation of grid-connected converters in unbalanced and distorted grids. The results obtained in this work will contribute to enhancing the stability of modern power systems that are getting more and more converter-dominated.

1. Introduction

In light of the recent developments around the net-zero carbon emission target by 2050, fossil fuels are slowly losing their position as the main source of electric energy generation [1,2]. The hazardous and harmful effects of fossil fuel-based energy generation are well documented [3,4]. Considering the role of fossil fuels on harmful gas emissions, researchers around the world made significant efforts to look for alternative sources of low-carbon electric power generation [5,6]. Out of various alternative solutions, renewable energy sources (RES) became very popular in recent times as they are abundant, clean, sustainable, and provide good economic value in the long-term. This gives rise to the modern electric power systems where RES-based distributed energy resources (DERs) are slowly starting to become a major supplier of electric power to the utility grid, thereby significantly reducing overall carbon emissions [7,8].

As the penetration of DERs is slowly increasing, efficient integration of these energy sources to the conventional power grid became a point

of major concern for electric utilities around the world [9]. DERs are typically connected to the grid through grid-connected converters (GCCs), thereby making the grid slowly converter-dominated [10,11]. It is to be noted here that high penetration of power converters will cause various adverse phenomena on the utility grid, especially in terms of power quality, reliability, voltage/frequency instability, etc. [12,13]. This motivated researchers to work on the control of GCCs to ensure efficient and grid-friendly integration of GCCs into the utility grid [14].

Efficient integration of DERs in a converter-dominated power grid is a very challenging task due to various power quality and voltage/frequency stability issues [15]. To mitigate these issues, extensive rules and grid codes (GCs) are developed by various regulating authorities around the world to ensure stable, safe, and continuous electric power transfer from DERs into the utility grid [16,17]. Grid codes are typically very extensive and cover many topics. Some of the popular requirements mentioned in the grid codes are power quality

* Corresponding author at: University of Brest, UMR CNRS 6027 IRDL, 29238 Brest, France.
E-mail address: Mohamed.Benbouzid@univ-brest.fr (M. Benbouzid).

<https://doi.org/10.1016/j.rser.2023.113508>

Received 14 January 2022; Received in revised form 8 June 2023; Accepted 26 June 2023

Available online 6 July 2023

1364-0321/© 2023 Elsevier Ltd. All rights reserved.

Nomenclature

$\Delta\omega$	Deviation from the nominal frequency
ΔP	Required power decrement
η	Frequency adaptation tuning gain
\hat{x}, \hat{z}	Estimated variables
A, A_z	State matrix
C, C_z	Output matrix
$L = [L_1 \ L_2]$	Observer gain matrix
ω, θ	Grid frequency and phase angle
ω_n	Nominal frequency
$v_{a,b,c}$	Line voltages
$v_{a,b,c}^\perp$	Orthogonal line voltages
$v_{i,a,b,c}$	Inverter output voltages
ϵ_{max}	Maximum line over-current
$i_{a,b,c}$	Line currents
i_{ref}	Current references
i_{th}	Threshold value of line currents
L	Line filter inductance
O	Observability matrix
P_0, P_{c2}, P_{s2}	Instantaneous and oscillating terms of active power
P_{max}	Maximal generator power
P_{nom}	Nominal generator power
P_{ref}, Q_{ref}	Active and reactive power references
$qv_{a,b,c}$	Quadrature line voltages
q_0, q_{c2}, q_{s2}	Instantaneous and oscillating terms of reactive power
Q_p	Reactive current ratio
R	Line filter resistance
T	Transformation matrix
V_g	Grid voltage level
$x^{+,-,0}$	Positive, negative, and zero sequences
$x^{p,n}$	Positive and negative components terms
$x_{d,q}$	Direct and quadrature axes terms
ANF	Adaptive notch filter
DC	Direct current
DERs	Distributed energy resources
FRT	Fault ride-through
GAO	Global adaptive observer
GCCs	Grid-connected converters
GCs	Grid codes
GNAO	Gain normalized adaptive observer
IGBT	Insulated gate bipolar transistor
LVRT	Low voltage ride-through
PCC	Point of common coupling

PI	Proportional integrator
PLL	Phase-locked loop
PNS	Positive and negative sequences
RES	Renewable energy sources
SAO	SOGI-type adaptive observer
SOGI	Second-order generalized integrator
STF	Self-tuning filter
SYRF	Synchronous reference frame
THD	Total Harmonic Distortion
VSI	Voltage source inverter

support strategy [22,23]. Grid voltage sags are categorized into two types, symmetrical when all phases have the same voltage level, and asymmetrical when the voltage levels of individual phases are unequal. Problems that arise due to symmetrical and asymmetrical voltage sags are summarized below [24,25]:

- Fault-induced high-current injection by the GCC may damage the IGBT switches due to over-current flow.
- Double fundamental frequency oscillation appears in the output power and the DC-link voltage of the GCC.
- DC-link voltage oscillations reduce the capacitor lifetime.
- DC-link voltage oscillations make the reference current non-sinusoidal, thereby deteriorating the power quality.

To mitigate the issues summarized above, symmetrical and asymmetrical LVRT capable control scheme development is essential. The LVRT capable control system must ensure some objectives that are, (1) reactive power injection to support the grid during voltage sags as per grid codes requirements [26], (2) active power curtailment depending on the fault depth [27], (3) real-time sequences extraction for negative sequence cancellation [28], (4) new current references calculation in both positive and negative sequences for double frequency active power oscillation mitigation under unbalanced sag [29,30], (5) limiting the injected currents to protect the inverter from over-current tripping [31], and (6) dual current controller ensuring the safe integration under a wide range of grid voltages [32]. Some recent results in this topic that satisfy some of these objectives can be found in [33,34].

It is to be noted here that in this work, our focus is on the LVRT control of grid-connected RES, where a GCC acts as an interface between the RES and the grid. In certain cases, e.g. doubly-fed induction generator (DFIG)-based grid-connected RES, the stator of DFIG is directly connected to the grid. This necessitates the development of DFIG-specific control approaches such as demagnetization control [35–37] and feed-forward control [38–40], which are typically not applicable to other types of grid-connection topology. As such, a detailed review of LVRT control system development for DFIG-based RES is avoided here and interested readers may consult the review papers [41–44], and the references therein for a comprehensive overview of this topic.

As highlighted in the LVRT objectives, dual-loop, i.e., positive and negative sequence controllers are essential to mitigate the adverse effects of asymmetrical voltage sags [45]. In order to facilitate the implementation of such controllers, fast and accurate frequency-adaptive sequence extraction of grid voltages and currents are essential. In this regard, several estimators are available in the literature. Some popular estimators are Kalman filter [46], demodulation [47,48], second-order generalized integrator (SOGI) [49], adaptive notch filter (ANF) [50], open-loop techniques [51], self-tuning filter (STF) [52], adaptive observers [53,54], to name a few. These estimators have their own merits and demerits.

These estimators operate by generating orthogonal signals from the measured three-phase voltages and currents. Then, by applying the symmetrical components theory [55], positive and negative sequence

standards at the point of common coupling (PCC) to the grid, active and reactive power regulation, voltage and frequency control, accurate grid-synchronization, fault ride-through (FRT) capability, etc. [18,19].

Out of the various requirements mentioned in the GCs, the focus of this work is particularly on the FRT capability. Momentary or short-term voltage fluctuations are very common in the utility grid. In practice, due to various faults, grid voltage amplitude may drop well below (e.g. 50%) the nominal value. Many GCs require that the DER be connected despite this large voltage drop/sag. As such, FRT ability in the form of low voltage ride-through (LVRT) capability should be embedded into the control system of GCCs [20,21]. This permits ensuring an uninterrupted grid integration even under large voltage sags and subsequently enhances the grid stability by voltage

components can easily be separated. Separated components can be used inside a traditional synchronous reference frame phase-locked loop (SYRF-PLL) [56] to make the overall operation grid frequency-adaptive. In the relevant literature, SOGI [49], ANF [50], and STF [52] are some of the most popular and widely used orthogonal signal generators. These filters use a linear harmonic oscillator model and based on this model the filtering task is performed. These filters have a band-pass property, which helps to reduce the effect of harmonics. However, the dynamic tuning range of these filters is limited if complex-conjugate poles are considered [57]. In the presence of noisy measurements, the Kalman filter [46] can be considered as a suitable orthogonal signal generator. However, it is difficult to tune, as it requires information about the process and measurement noise characteristics. Moreover, it is also computationally demanding for real-time applications [58]. In this context, adaptive observer-based sequence extraction techniques can be considered as a suitable choice since these observers have very fast convergence properties [53,54] unlike second-order band-pass type filters. Moreover, they are not computationally demanding like the Kalman filter and can be tuned easily using pole placement. As such, in this work, adaptive observers have been considered as the positive and negative sequence extraction techniques.

In a recent work [28,59], a comparative analysis has been presented to show the suitability of these adaptive observer-based sequence extraction techniques on synthetic grid voltages. This motivated the present work of making a systematic comparison of these techniques to provide LVRT capabilities into the control system of GCCs. For this purpose, sequence extraction-based current controllers are adopted in this work, which is motivated by [60]. The key features of this work are summarized as follows:

- A control solution is proposed for ensuring reactive power injection as a priority to alleviate the negative effects of voltage sag. The reactive power set-point is determined as per GCs requirements, ensuring stable and reliable grid operation.
- The injected currents are limited within a threshold value under balanced or unbalanced sags, which helps avoid converter over-current-related tripping. Thus, the proposed solution ensures system stability and prevents unnecessary interruptions in power delivery.
- The current limiting property is based on reducing the active power reference while maintaining the reactive power reference within GCs requirements. This proposed approach optimizes the power flow within the maximum inverter capacity and ensures compliance with grid regulations.
- Grid voltage sequences and their angular frequency are synthesized using the studied adaptive observers. This proposed feature offers an improved estimation and control framework compared to conventional approaches, leading to enhanced performance and robustness in grid-connected inverter systems.
- A detailed formulation is provided to calculate current references in the synchronous reference frame (SYRF) in both positive and negative sequences (PNS). This formulation enables the suppression of active output power oscillations, which is crucial for maintaining grid stability and avoiding DC-link voltage fluctuations leading to capacitors damage.
- Actual current sequences are obtained through the designed adaptive observers and then controlled separately using a dual-controller approach to achieve all the LVRT common options. By employing these adaptive observers, accurate estimation and flexible current control are ensured, thereby enabling an effective LVRT implementation and grid synchronization under various grid faulty conditions.

The rest of this paper is organized as follows: Section 2 introduces the used system with its modeling in SYRF-coordinate. Moreover, all GCCs control requirements are also detailed here. In Section 3, details of the grid-synchronizing PNS extraction techniques are given.

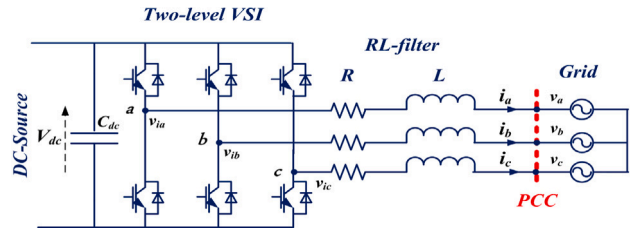


Fig. 1. Three-phase distributed grid-connected renewable energy system.

Table 1
System parameters.

Parameters	Symbol	Value
Nominal power	P_{nom}	500 W
DC link	V_{dc}	200 V
Grid voltage	V_g^{rms}	110 V
Grid frequency	f_g	50 Hz
Switching frequency	f_{sw}	10 kHz
Filter resistance	R	0.3 Ω
Filter inductance	L	11 mH
Sampling time	T_s	0.05 ms

Comprehensive numerical simulation results using various challenging LVRT scenarios are provided in Section 4. Details of the laboratory-scale hardware setup and extensive experimental results are provided in Section 5. Finally, Section 7 concludes the paper.

2. Overview of the studied system

2.1. System description

Fig. 1 shows the overview of the considered system. It is composed of a two-level voltage source inverter (VSI) which is typically powered by a direct current (DC) source to emulate the RES. The VSI is then connected to the main grid at the point of common coupling (PCC) through the output filter, which is inductive in our case. All the system parameters are listed in Table 1.

By applying Kirchhoff's laws to the circuit in Fig. 1, the following relationships between the electrical parameters are obtained:

$$\begin{cases} L \frac{di_a}{dt} = v_{i_a} - v_a - Ri_a \\ L \frac{di_b}{dt} = v_{i_b} - v_b - Ri_b \\ L \frac{di_c}{dt} = v_{i_c} - v_c - Ri_c \end{cases} \quad (1)$$

where v_a, v_b, v_c are the grid phase voltages, $v_{i_a}, v_{i_b}, v_{i_c}$ are the inverter output phase voltages. i_a, i_b, i_c are the grid line currents, L is the line filter inductor, and R is the parasitic resistance of the line inductor.

In order to study the system under generic grid voltages, i.e., balanced or unbalanced situations, both PNS should be considered. Considering the simplicity of the SYRF in grid-connected converters control [1], Eq. (1) is transformed in SYRF by taking into account both PNS:

$$\begin{cases} L \frac{di_d^p}{dt} = -Ri_d^p + L\omega i_q^p + v_{i_d}^p - v_d^p \\ L \frac{di_q^p}{dt} = -Ri_q^p - L\omega i_d^p + v_{i_q}^p - v_q^p \\ L \frac{di_d^n}{dt} = -Ri_d^n - L\omega i_q^n + v_{i_d}^n - v_d^n \\ L \frac{di_q^n}{dt} = -Ri_q^n + L\omega i_d^n + v_{i_q}^n - v_q^n \end{cases} \quad (2)$$

where subscripts d and q represent the direct and quadrature axes of SYRF, superscripts p and n represent the positive and negative sequence

components of voltage and currents. The delivered powers can then be written as [61]:

$$\begin{cases} p(t) = p_0 + p_{c2} \cos(2\omega t) + p_{s2} \sin(2\omega t) \\ q(t) = q_0 + q_{c2} \cos(2\omega t) + q_{s2} \sin(2\omega t) \end{cases} \quad (3)$$

where p_0 and q_0 represent the instantaneous active and reactive powers. Under the fault-free state, p_0 and q_0 are constants and correspond to active and reactive power references without any oscillations. The oscillating terms p_{c2} , p_{s2} , q_{c2} , and q_{s2} appear only under the unbalanced grid voltages. All the terms in Eq. (3) are expressed as:

$$\begin{bmatrix} p_0 \\ p_{c2} \\ p_{s2} \\ q_0 \\ q_{c2} \\ q_{s2} \end{bmatrix} = \frac{3}{2} \begin{bmatrix} v_d^p & v_q^p & v_d^n & v_q^n \\ v_d^n & v_q^n & v_d^p & v_q^p \\ v_q^n & -v_d^n & -v_q^p & v_d^p \\ v_q^p & -v_d^p & v_q^n & -v_d^n \\ v_q^n & -v_d^n & v_q^p & -v_d^p \\ -v_d^n & -v_q^n & v_d^p & v_q^p \end{bmatrix} \begin{bmatrix} i_d^p \\ i_q^p \\ i_d^n \\ i_q^n \end{bmatrix} \quad (4)$$

2.2. Control requirements

In order to avoid the disconnection of GCCs from the utility grid under symmetrical or asymmetrical voltage sags, the control structure must meet some requirements to ride through this fault. These requirements are summarized below:

- **Current-limiting control:** Peak current limiter-enabled LVRT control is necessary to improve the grid stability under voltage sags, protect the inverter and the semiconductor switches from over-current damages, ignore active power oscillations under unbalanced faults, and ensure a continuous grid connection even under faulty grid conditions.
- **Reactive power injection:** The designed control architecture is focused mainly on reactive power injection as per GCs to support the grid during voltage sags, generate new current references on SYRF dealing with active power fluctuations, and maintain the injected currents below the threshold value even under balanced or unbalanced faults.

These control requirements are achieved through the control structure shown in Fig. 2. The remainder of this Section provides the details of individual blocks while the details of PNS extraction techniques are given in Section 3.

2.2.1. Grid code requirements

Active and reactive power references are determined based on the grid voltage level. Under normal operation (i.e. V_g (p.u.) = 1), injected active power corresponds exactly to the nominal value of the GCCs with the reactive power being zero, i.e., $P_{ref} = P_{nom}$, $Q_{ref} = 0$ VAR. However, under grid voltage sags (V_g (p.u.) < 1), recent GCs mandate reactive power injection to support the grid voltage and enhance its stability [26].

As shown in Fig. 3, the required reactive current is selected as a function of the rated converter current. This relationship is mainly based on the voltage level as expressed in the following equation:

$$Q_p = \begin{cases} 1, & 0 \leq V_g < 0.5 \\ 2(1 - V_g), & 0.5 \leq V_g < 0.9 \\ 0, & 0.9 \leq V_g < 1.1 \end{cases} \quad (5)$$

The new reactive power reference is therefore defined as:

$$Q_{ref} = Q_p \cdot P_{max} \quad (6)$$

where P_{max} is the full available power of the generator.

2.2.2. Current reference generation

As previously mentioned, unbalanced faults generate double the fundamental grid-frequency active power oscillations. These oscillations should be eliminated to facilitate smooth grid integration of the RES. For this issue, SYRF reference currents are determined based on Eq. (4) by forcing both p_{c2} and p_{s2} to become zero:

$$\begin{bmatrix} i_{dref}^p \\ i_{qref}^p \\ i_{dref}^n \\ i_{qref}^n \end{bmatrix} = \frac{2}{3} \begin{bmatrix} v_d^p & v_q^p & v_d^n & v_q^n \\ v_d^n & v_q^n & v_d^p & v_q^p \\ v_q^n & -v_d^n & -v_q^p & v_d^p \\ v_q^p & -v_d^p & v_q^n & -v_d^n \end{bmatrix}^{-1} \begin{bmatrix} P_{ref} \\ 0 \\ 0 \\ Q_{ref} \end{bmatrix} \quad (7)$$

where, P_{ref} and Q_{ref} represent the active and reactive power references, respectively. Q_{ref} is selected using the grid code requirements, while P_{ref} is determined based on the active power curtailment process when the injected currents must be limited to the threshold value [31,62]. Therefore, the current references represented in SYRF are expressed as [60,63]:

$$\begin{bmatrix} i_{dref}^p \\ i_{qref}^p \\ i_{dref}^n \\ i_{qref}^n \end{bmatrix} = \frac{2P_{ref}}{3A} \begin{bmatrix} v_d^p \\ v_q^p \\ -v_d^n \\ -v_q^n \end{bmatrix} + \frac{2Q_{ref}}{3B} \begin{bmatrix} v_d^p \\ -v_q^p \\ v_d^n \\ -v_q^n \end{bmatrix} \quad (8)$$

where,

$$A = (v_d^p)^2 + (v_q^p)^2 - (v_d^n)^2 - (v_q^n)^2$$

$$B = (v_d^p)^2 + (v_q^p)^2 + (v_d^n)^2 + (v_q^n)^2$$

2.2.3. Current limiting process

The main purpose of the current limiter is to enhance the protective measures for the GCCs under faulty conditions. The current controller should prohibit the line currents to exceed their threshold value, which is defined as the maximum permissible peak line currents. The equation that describes this process in the natural reference frame is as follows [64]:

$$i_j^{ref} = \begin{cases} i_{th} & |i_j^{ref}| > i_{th} \\ -i_{th} & |i_j^{ref}| < -i_{th} \\ i_j^{ref} & \text{otherwise} \end{cases} \quad (9)$$

where, $j = a, b, c$ denote the individual phases and i_{th} is the threshold value of line-currents. i_{th} is considered as 1.5 p.u. in this paper.

Considering a sinusoidal signal $x(t)$ with an angular frequency ω , magnitude A , and a phase shift ϕ , each line-currents can be expressed as follows:

$$x(t) = A \cos(\omega t + \phi) \quad (10)$$

Since the main issue in the current limiting implementation is the accurate magnitude calculation, the estimator considered in [62] is used here as it is fast and easy to implement:

$$A = \sqrt{(x(t))^2 + \frac{1}{\omega^2} \left(\frac{dx(t)}{dt} \right)^2} \quad (11)$$

As explained in [31], the used current limiter is based on current magnitude regulation to the threshold value. This is achieved firstly by converting the obtained current references into the natural reference frame and computing their magnitudes. Moreover, to consider both balanced and unbalanced situations, this limiter selects the maximum line currents and calculates its error regarding the threshold value. Thus, the following equation is obtained:

$$\varepsilon_{max} = \max(A_{i_a}, A_{i_b}, A_{i_c}) - i_{th} \quad (12)$$

Since the reactive power reference is selected by the grid codes, the only way to limit the line currents is to decrease the active power

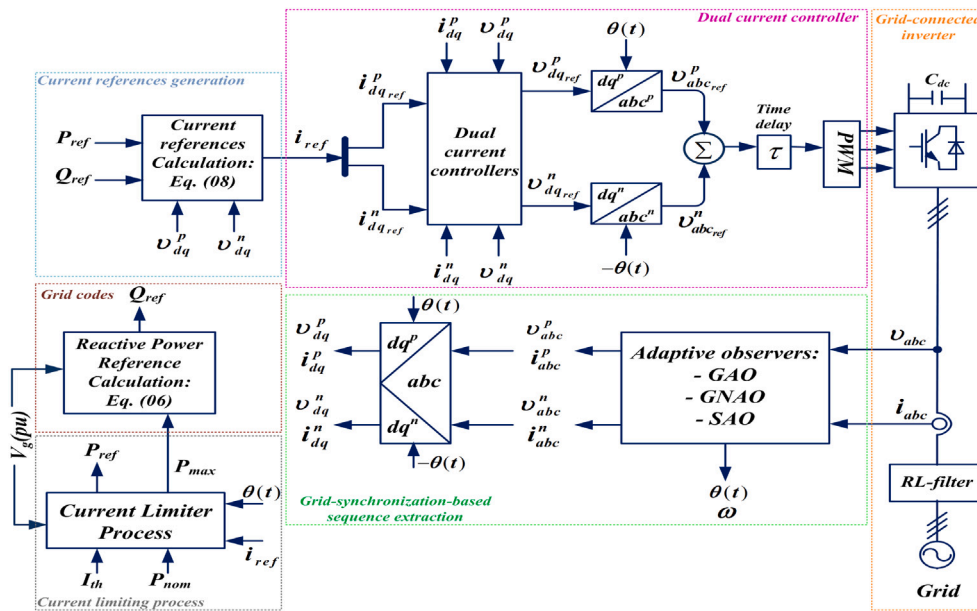


Fig. 2. Block diagram of the proposed control strategy.

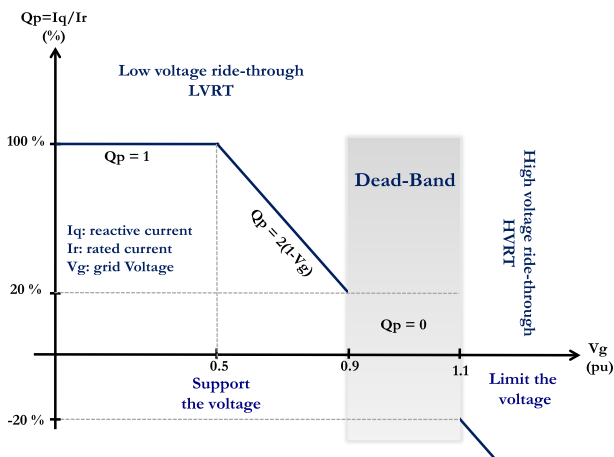


Fig. 3. Reactive current injection to support/limit voltage during low voltage ride-through/high voltage ride-through.

reference and observe its effect in the line-current magnitudes. The required power that should be reduced (ΔP) is determined via a simple integral controller with tuning gain k_i :

$$\Delta P = k_i \int \epsilon_{max} \cdot dt \quad (13)$$

In this case, the new active power reference can be expressed mathematically as:

$$P_{ref} = P_{nom} - \Delta P \quad (14)$$

It should be mentioned that under severe voltage sags, currents increase excessively, and ΔP will be higher than P_{nom} . In this case, the full available power of the generator P_{max} should be reduced and the power references can be calculated as follows:

$$\begin{cases} P_{ref} = 0 \\ P_{max} = 2 \cdot P_{nom} - \Delta P \\ Q_{ref} = Q_p \cdot P_{max} \end{cases} \quad (15)$$

2.2.4. Dual current controller

The adopted current controller shown in Fig. 4 is working at SYRF using proportional integrator (PI) regulators. The duality concept concerns the PNS control simultaneously, i.e., under normal grid voltages, injected power references are ensured only by regulating the positive currents. However, under faulty grid voltages, it is necessary to control the negative currents and eliminate the active power oscillations.

According to the power reference values, the current references are determined based on Eq. (8). These currents are then regulated via PI controllers, added to the feedforward and cross-coupling terms, the obtained commands are sent to the inverter through a pulse width modulation block [31,65]. For the controller, the objective is to achieve zero steady-state tracking error, i.e., $\lim_{t \rightarrow \infty} (i_{dqref}^m - i_{dq}^m) = 0, m \in \{p, n\}$, where *ref* indicates the reference value and the i_{dq}^m are obtained through the sequence estimators detailed in Section 3.

2.2.5. Grid-synchronization-based sequence extraction

In order to achieve better control of active and reactive powers under balanced or unbalanced grid voltages, accurate grid frequency estimation and voltages/currents sequences extraction are necessary. As discussed in the Introduction section, to address this issue, several estimators have been proposed in the literature. The focus of the present paper is to make a systematic comparison of adaptive observer-based sequence extraction techniques in LVRT capabilities improvement. The following section discusses in detail these techniques.

Sequence separation is also important to quantify the voltage fault level and therefore apply the grid code requirements. The equation that describes this quantification is given as follows [66]:

$$V_g(pu) = \frac{v_d^p}{v_{nom}^{peak}} \quad (16)$$

where, $v_{nom}^{peak} = \sqrt{\frac{2}{3}} \cdot V_g^{rms}$, and v_d^p is obtained using voltage sequences estimator.

3. Adaptive observer-based grid-synchronization

Grid voltages in a generic (symmetrical/asymmetrical) form are composed of positive (+), negative (-), and zero (0) sequence components. Since the studied system represents a three-leg three-wire inverter, the zero (0) sequence component has no impact on the system

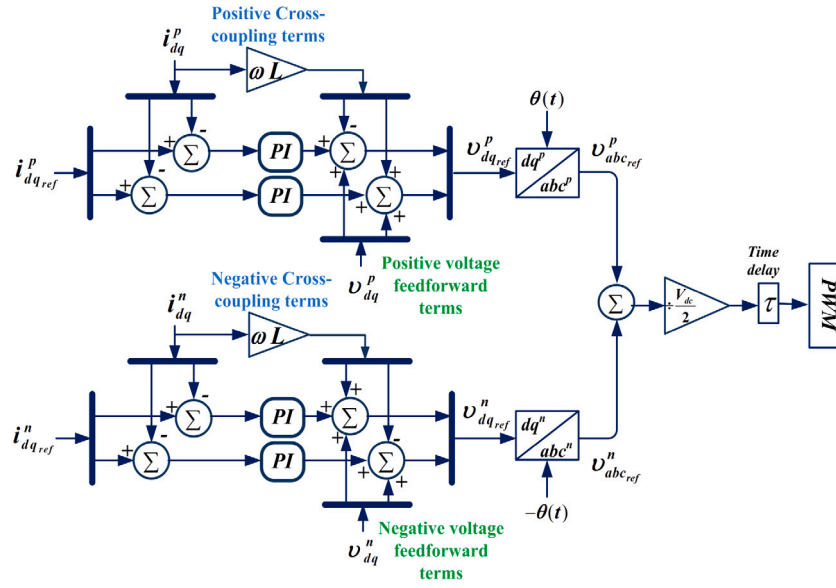


Fig. 4. Overview of the used dual current controller.

control [67]. Therefore, the three-phase grid voltages in our case are expressed as:

$$\begin{cases} v_a = \underbrace{A^+ \sin(\omega t + \phi^+)}_{v_a^+} + \underbrace{A^- \sin(\omega t + \phi^-)}_{v_a^-} \\ v_b = \underbrace{A^+ \sin(\omega t - \frac{2\pi}{3} + \phi^+)}_{v_b^+} + \underbrace{A^- \sin(\omega t + \frac{2\pi}{3} + \phi^-)}_{v_b^-} \\ v_c = \underbrace{A^+ \sin(\omega t + \frac{2\pi}{3} + \phi^+)}_{v_c^+} + \underbrace{A^- \sin(\omega t - \frac{2\pi}{3} + \phi^-)}_{v_c^-} \end{cases} \quad (17)$$

where $A \in \mathbb{R}_{\geq 0}$ represents the magnitude, $\phi \in \mathbb{R}$ is the initial phase shift, and $\omega \in \mathbb{R}_{> 0}$ is the angular frequency. It should be noted that according to the European standard EN 50160, the frequency can vary between 47 and 52 Hz [68]. In the same way, the injected currents are expressed in their steady state. The following development concerns the grid voltages only and will be generalized also to the injected currents.

In order to extract both positive (+) and negative (-) sequences, and estimate the angular frequency ω from Eq. (17), it should be necessary to define the quadrature version of the grid voltages:

$$\begin{cases} qv_a = \underbrace{A^+ \cos(\omega t + \phi^+)}_{qv_a^+} + \underbrace{A^- \cos(\omega t + \phi^-)}_{qv_a^-} \\ qv_b = \underbrace{A^+ \cos(\omega t - \frac{2\pi}{3} + \phi^+)}_{qv_b^+} + \underbrace{A^- \cos(\omega t + \frac{2\pi}{3} + \phi^-)}_{qv_b^-} \\ qv_c = \underbrace{A^+ \cos(\omega t + \frac{2\pi}{3} + \phi^+)}_{qv_c^+} + \underbrace{A^- \cos(\omega t - \frac{2\pi}{3} + \phi^-)}_{qv_c^-} \end{cases} \quad (18)$$

As it is clear from Eqs. (17) and (18), the PNS of the grid voltages can be determined using the following equations:

$$\begin{bmatrix} v_a^+ \\ v_b^+ \\ v_c^+ \end{bmatrix} = \frac{1}{3} \begin{bmatrix} 1 & -\frac{1}{2} & -\frac{1}{2} \\ -\frac{1}{2} & 1 & -\frac{1}{2} \\ -\frac{1}{2} & -\frac{1}{2} & 1 \end{bmatrix} \begin{bmatrix} v_a \\ v_b \\ v_c \end{bmatrix} + \frac{1}{2\sqrt{3}} \begin{bmatrix} 0 & 1 & -1 \\ -1 & 0 & 1 \\ 1 & -1 & 0 \end{bmatrix} \begin{bmatrix} qv_a \\ qv_b \\ qv_c \end{bmatrix}, \quad (19)$$

$$\begin{bmatrix} v_a^- \\ v_b^- \\ v_c^- \end{bmatrix} = \frac{1}{3} \begin{bmatrix} 1 & -\frac{1}{2} & -\frac{1}{2} \\ -\frac{1}{2} & 1 & -\frac{1}{2} \\ -\frac{1}{2} & -\frac{1}{2} & 1 \end{bmatrix} \begin{bmatrix} v_a \\ v_b \\ v_c \end{bmatrix} - \frac{1}{2\sqrt{3}} \begin{bmatrix} 0 & 1 & -1 \\ -1 & 0 & 1 \\ 1 & -1 & 0 \end{bmatrix} \begin{bmatrix} qv_a \\ qv_b \\ qv_c \end{bmatrix}. \quad (20)$$

As observed in Eqs. (19) and (20), the quadrature signals are necessary to determine the sequence components. In general, if the grid frequency is known, then, the quadrature signals can be obtained easily by applying a 90° phase shift on the original signals. This is equivalent to delaying the original signals by one quarter of the fundamental cycle. However, the grid frequency is unknown in practice. This motivated us to apply adaptive observer-based grid-synchronization techniques from the literature. These observers consider the grid voltages and the corresponding quadrature components as the state variables, while the grid frequency appears as an unknown parameter in the system dynamics. From the estimated parameter and state variables, the PNS components can be easily extracted in real-time by applying Eqs. (19) and (20). Details of the adopted frequency-adaptive observers are given in the following:

3.1. Global adaptive observer

The estimation principle based on the global adaptive observer (GAO) is detailed in [69]. In order to define the state-space model of the studied system, only phase “a” voltage is considered. Then, the developed model is generalized to the other phase voltages and also for the injected currents. The following state variables $x_1, x_2 \in \mathbb{R}$ are considered:

$$\begin{cases} x_1 = v_a = A^+ \sin(\omega t + \phi^+) + A^- \sin(\omega t + \phi^-) \\ x_2 = \dot{x}_1 = \dot{v}_a = \omega(A^+ \cos(\omega t + \phi^+) + A^- \cos(\omega t + \phi^-)) \end{cases} \quad (21)$$

According to Eq. (21), the continuous-time system model is expressed as:

$$\begin{cases} \dot{x}(t) = Ax(t) \\ y(t) = Cx(t) \end{cases} \quad (22)$$

where the state matrix $A \in \mathbb{R}^{2 \times 2}$, output matrix $C \in \mathbb{R}^{1 \times 2}$, and the state vector $x \in \mathbb{R}^{2 \times 1}$ are given by:

$$A = \begin{bmatrix} 0 & 1 \\ -\omega^2 & 0 \end{bmatrix}, \quad C = [1 \quad 0], \quad \text{and } x = [x_1 \quad x_2]^T.$$

Since the grid frequency ω is an unknown variable in the state matrix A , it is formulated in terms of the nominal grid frequency ($\omega_n =$

100π) as $\omega^2 = \eta\omega_n^2$, $\eta \in \mathbb{R}_{>0}$. This permits simplifying the adaptation law development of the grid frequency ω [53,69]. The problem here is to estimate the state vector $x(t)$ from the measured output signal $y(t)$. Since the considered system is linear time-invariant in nature with an unknown parameter, this can be easily achieved by the conventional linear Luenberger observer together with an adaptation law for the unknown parameter. Before developing the observer, first, the observability of the system needs to be confirmed. In order to study the observability of the system presented by Eq. (22), the observability matrix O should be given:

$$O = \begin{bmatrix} C \\ CA \end{bmatrix} = \begin{bmatrix} 1 & 0 \\ 0 & 1 \end{bmatrix} \quad (23)$$

As it is clear from Eq. (23), the rank of the matrix O is 2 which is the same as the state matrix A . Thus, the system expressed by Eq. (22) is observable. The GAO design is provided in detail in [28,69], which is based on the following coordinate transformation:

$$z = Tx \quad (24)$$

where $z = [z_1 \ z_2]^T \in \mathbb{R}^{2 \times 1}$ is the transformed state vector. The non-singular transformation matrix $T \in \mathbb{R}^{2 \times 2}$ is given below:

$$T = \frac{(1 + \eta)^{-1}}{\omega_n^2} \begin{bmatrix} 1 & -\frac{1}{\omega_n} \\ \eta\omega_n & 1 \end{bmatrix}.$$

The new system matrices $A_z \in \mathbb{R}^{2 \times 2}$ and $C_z \in \mathbb{R}^{1 \times 2}$ are obtained as $A_z = TAT^{-1} = A$, $C_z = CT^{-1} = [\omega_n^2 \ \omega_n]$. Therefore, the transformed state-space model for the phase voltage v_a is formulated as:

$$\begin{cases} \dot{z}(t) = A_z z(t) \\ v_a(t) = C_z z(t) \end{cases} \quad (25)$$

The objective here is to estimate the states and the unknown grid frequency parameter with zero steady-state error from the measured grid voltage, i.e., $\lim_{t \rightarrow \infty} (z - \hat{z}) = 0$ and $\lim_{t \rightarrow \infty} (\omega - \hat{\omega}) = 0$, where $\hat{\cdot}$ represents the estimated value. For this purpose, the Luenberger observer [70] is employed to estimate the phase voltage v_a of the system presented by Eq. (25) as follows:

$$\dot{\hat{z}} = \hat{A}_z \hat{z} + \mathcal{L} (v_a - \hat{v}_a) \quad (26)$$

where \hat{z} and \hat{v}_a are the estimated state variables and the a phase voltage, respectively. The observer gain is given by the matrix $\mathcal{L} \in \mathbb{R}^{2 \times 1}$. Moreover, \hat{A}_z contains the estimated grid frequency term in the function of the nominal one as $\hat{A}_z = \begin{bmatrix} 0 & 1 \\ -\hat{\eta}\omega_n^2 & 0 \end{bmatrix}$.

Using the Lyapunov approach, the stability and convergence analysis of this observer are studied in detail in [69]. Based on the Lyapunov function analysis in [69], the following frequency update law makes the overall system globally asymptotically stable:

$$\dot{\hat{\eta}} = -\gamma\omega_n^2 (v_a - \hat{v}_a) \hat{z}_1, \quad (27)$$

where the frequency update law tuning gain is given by the positive constant γ . Since the transformed state variables are available, the phase voltage v_a and its quadrature signal qv_a can be obtained through the following formula:

$$\hat{x} = \hat{T}^{-1} \hat{z} \quad (28)$$

where

$$\hat{T}^{-1} = \omega_n^2 \begin{bmatrix} 1 & \frac{1}{\omega_n} \\ -\hat{\eta}\omega_n & 1 \end{bmatrix}.$$

In the same manner, the other phase voltages v_b and v_c with their quadrature signals qv_b and qv_c are estimated. Through the Eqs. (19) and (20), positive and negative voltage sequences can be determined. The above development is generalized to the injected currents (i_a, i_b, i_c) to obtain the current sequence components and permit the dual current control process. Since the grid frequency is the same for voltage and currents, only one frequency update law is enough for voltage and currents.

3.2. Gain normalized adaptive observer

As highlighted in [53], the GAO has a longer convergence time in the presence of voltage sags due to the lack of gain normalization in the frequency update law. To overcome this issue, a gain normalized adaptive observer (GNAO) is proposed there, which is detailed in the following:

The same system model of Eq. (22) is employed for this observer. To consider the gain normalization in the frequency law estimation, the unknown frequency ω is formulated as: $\omega = \omega_n + \Delta\omega$, where $\Delta\omega \in \mathbb{R}$ is the frequency shift from its nominal value. Considering this new grid frequency formulation, the non-singular states transformation is given as:

$$z = Tx \quad (29)$$

where $T = \frac{1}{2\omega^3} \begin{bmatrix} \omega & -1 \\ \omega^2 & \omega \end{bmatrix}$. The system model is then expressed in the z -coordinate as:

$$\begin{cases} \dot{z}(t) = A_z z(t) \\ v_a(t) = C_z z(t) \end{cases} \quad (30)$$

where the new system matrices $A_z \in \mathbb{R}^{2 \times 2}$ and $C_z \in \mathbb{R}^{1 \times 2}$ are obtained as: $A_z = TAT^{-1} = A$, $C_z = CT^{-1} = [\omega^2 \ \omega]$. Similar to the previous observer, the objective here is to estimate the states and the unknown grid frequency parameter with zero steady-state error from the measured grid voltage, i.e., $\lim_{t \rightarrow \infty} (z - \hat{z}) = 0$ and $\lim_{t \rightarrow \infty} (\omega - \hat{\omega}) = 0$. For this purpose, the Luenberger observer is applied to estimate the phase voltage v_a and its quadrature signal qv_a as follows:

$$\dot{\hat{z}} = \hat{A}_z \hat{z} + \mathcal{L} (v_a - \hat{v}_a) \quad (31)$$

where $\mathcal{L} \in \mathbb{R}^{2 \times 1}$ with $\mathcal{L} = [\mathcal{L}_1 \ \mathcal{L}_2]^T$ represents the observer gain matrix and

$$\hat{A}_z = \begin{bmatrix} 0 & 1 \\ -(\omega_n + \Delta\omega)^2 & 0 \end{bmatrix}.$$

Utilizing the concept of the frequency-locked loop, the following dynamic frequency estimation law is obtained in [53]:

$$\dot{\Delta\omega} = -\frac{\gamma(\mathcal{L}_1 + \mathcal{L}_2)\hat{\omega}^3 \hat{z}_1 (v_a - \hat{v}_a)}{\sqrt{\frac{(\hat{z}_1 2\hat{\omega}^3)^2 + (\hat{z}_2 2\hat{\omega}^2)^2}{2\hat{\omega}^2}}} \quad (32)$$

where the constant $\gamma \in \mathbb{R}_{>0}$ is the tunable frequency identification gain. The gain introduced in the denominator of Eq. (32) normalizes the frequency estimation law by the estimated grid voltage magnitude. This gain permits achieving a good frequency estimation even in the presence of deep voltage sags [28,53]. The stability analysis of this observer and the parameters tuning are studied in detail in [53] by adopting the Routh–Hurwitz criterion. Similarly to GAO, the phase voltage v_a and its quadrature signal qv_a can be obtained through the following transformation:

$$\hat{x} = \hat{T}^{-1} \hat{z} \quad (33)$$

$$\text{where, } \hat{T}^{-1} = \begin{bmatrix} \hat{\omega}^2 & \hat{\omega} \\ -\hat{\omega}^3 & \hat{\omega}^2 \end{bmatrix}.$$

All grid voltages and currents will be determined in the same way using the observer of Eq. (31). Positive and negative sequences are then obtained through Eqs. (19) and (20).

3.3. SOGI-type adaptive observer

Contrary to the previous observers, SOGI-type adaptive observer (SAO) employs another system model with new state variables $x_1, x_2 \in \mathbb{R}$ and state vector $x \in \mathbb{R}^{2 \times 1}$ with $x = [x_1 \ x_2]$ that are expressed as [54]:

$$\begin{cases} x_1 = v_a^+ = -A^+ \cos(\omega t + \phi^+) - A^- \cos(\omega t + \phi^-) \\ x_2 = v_a = A^+ \sin(\omega t + \phi^+) + A^- \sin(\omega t + \phi^-) \end{cases} \quad (34)$$

The grid phase voltage v_a is formulated by the following dynamic system model:

$$\begin{cases} \dot{x}(t) = \mathcal{A}x(t) \\ v_a(t) = Cx(t) \end{cases} \quad (35)$$

where $\mathcal{A} = \begin{bmatrix} 0 & \omega \\ -\omega & 0 \end{bmatrix}$, $C = [0 \quad 1]$.

In order to confirm the observability of the system given by Eq. (35), the rank of observability matrix O should be the same as the state matrix \mathcal{A} rank. As observed in the following expression, the matrix O is of rank 2, therefore the system is observable:

$$O = \begin{bmatrix} C \\ C\mathcal{A} \end{bmatrix} = \begin{bmatrix} 0 & 1 \\ -\omega & 0 \end{bmatrix} \quad (36)$$

Similar to the design method used in the previous observers, the non-singular transformation is represented as:

$$z = Tx \quad (37)$$

where $T = \frac{1}{2\omega} \begin{bmatrix} 1 & 1 \\ -1 & 1 \end{bmatrix}$. The obtained system is expressed in z-coordinate as:

$$\begin{cases} \dot{z}(t) = \mathcal{A}_z z(t) \\ v_a(t) = C_z z(t) \end{cases} \quad (38)$$

where the new system matrices $\mathcal{A}_z \in \mathbb{R}^{2 \times 2}$ and $C_z \in \mathbb{R}^{1 \times 2}$ are obtained as: $\mathcal{A}_z = T\mathcal{A}T^{-1} = A$, $C_z = CT^{-1} = [\omega \quad \omega]$. Similar to the previous observers, the objective here is to estimate the states and the unknown grid frequency parameter with zero steady-state error from the measured grid voltage, i.e., $\lim_{t \rightarrow \infty} (z - \hat{z}) = 0$ and $\lim_{t \rightarrow \infty} (\omega - \hat{\omega}) = 0$. For this purpose, the following Luenberger observer is applied to the system states given by Eq. (38):

$$\dot{\hat{z}} = \hat{\mathcal{A}}_z \hat{z} + \mathcal{L} (v_a - \hat{v}_a) \quad (39)$$

where $\mathcal{L} \in \mathbb{R}^{2 \times 1}$ with $\mathcal{L} = [\mathcal{L}_1 \quad \mathcal{L}_2]^T$ is the observer gain matrix. In addition, the observer states matrix is given by the following equation:

$$\hat{\mathcal{A}}_z = \begin{bmatrix} 0 & \omega_n + \hat{\Delta}\omega \\ -(\omega_n + \hat{\Delta}\omega) & 0 \end{bmatrix}.$$

The gain normalized frequency update law in this case is given by:

$$\dot{\hat{\Delta}\omega} = -\frac{\gamma (\mathcal{L}_1 + \mathcal{L}_2) \hat{\omega} \hat{z}_1 (v_a - \hat{v}_a)}{\hat{z}^T \hat{z}} \quad (40)$$

where the constant $\gamma \in \mathbb{R}_{>0}$ is a tuning parameter. Details of the observer design and local stability analysis can be found in [54]. Given the estimated state variables z , the individual phase voltage v_a and its orthogonal signal v_a^+ can be evaluated using the following transformation:

$$\hat{x} = \hat{T}^{-1} \hat{z} \quad (41)$$

where, $T^{-1} = \hat{\omega} \begin{bmatrix} 1 & -1 \\ 1 & 1 \end{bmatrix}$.

The same development is applied to other phase voltages and currents. Through the Eqs. (19) and (20), positive and negative sequences of the voltages and currents are calculated for further use. An overview of the adaptive observer-based sequence extraction strategies adopted in this work is given in Fig. 5.

3.4. Frequency domain analysis of the sequence extraction techniques

The estimators presented in this Section assume that the grid has only a fundamental frequency component. However, in practice, harmonic signals are often unavoidable. European standard EN 50160 [68] specifies the acceptable harmonics limit in the grid voltage. According to this and various other international standards, a total harmonic distortion (THD) of 5% is often allowed. As such, sequence extraction techniques should also be able to work properly in a distorted grid. In the grid-synchronization literature, frequency domain analysis is

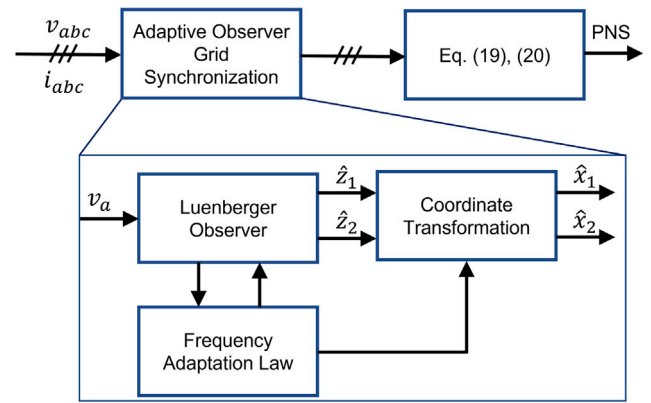


Fig. 5. A general overview of the adaptive observer-based sequence extraction strategy.

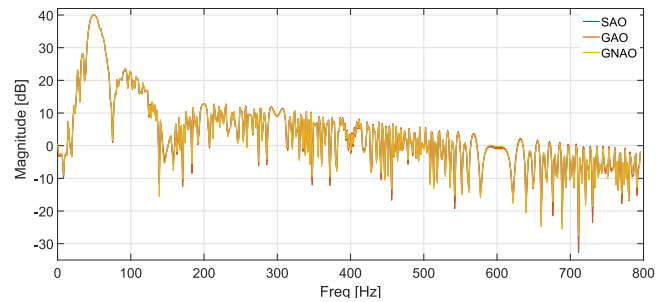


Fig. 6. Frequency response of the selected sequence extraction techniques.

the de facto standard for harmonic robustness analysis. The estimators presented in this Section are nonlinear in nature. As such, two approaches can be considered for the linear analysis of the estimators. In the first case, the analytical approach is used by developing a small-signal model of the estimators. However, it often requires several assumptions. In the second method, a numerical approach is used through frequency response estimation. The second approach is widely popular due to ease of obtaining the frequency response using numerical simulation only. As such, this approach is considered here.

To obtain the frequency response, first the estimator gains need to be tuned. To ensure fair tuning, all the observers are tuned to have a similar dynamic response when subject to step-change in the grid frequency. Through numerical simulation, it has been found that $\mathcal{L} = [0.0012 \quad 2.6250]$ for both GAO and GNAO, and $\mathcal{L} = [0.3750 \quad 2.6250]$ for SAO can provide similar dynamic response. Moreover, the value of γ is considered as 1000, 150, and 0.2 for GAO, GNAO, and SAO, respectively to have roughly two-cycle convergence time. These values are also used in the subsequent Sections.

To obtain the frequency response, a sine stream signal with frequency range 1 – 5000 [rad/s] and amplitude of 0.01 is added as a perturbation to the base input signal of amplitude 1 and frequency 50 Hz. The Bode magnitude plot of the three estimators for the transfer function $\hat{y}(s)/y(s)$ can be found in Fig. 6. The frequency response plot shows that the three estimators have similar frequency responses, and they show band-pass filtering properties around the fundamental grid frequency. This is particularly important as the sequence estimators need to extract the fundamental component of the voltage/current from the measured harmonically distorted signals. The accuracy of sequence extraction plays an important role in ultimately achieving a lower THD, thereby improving the efficiency of the system.

4. Simulation results

In order to achieve a comparative analysis of the observers detailed above in the closed-loop LVRT application, extensive simulation studies

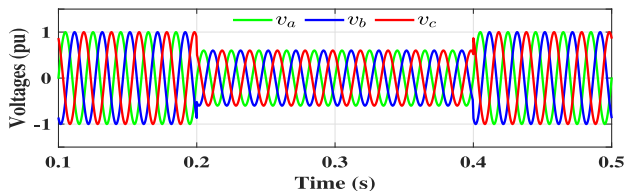


Fig. 7. Grid voltages during the balanced voltage sag test.

are considered. The system parameters are listed in Table 1, which are employed in both simulation and experimental tests. To verify each observer and show its dynamic response in the presence of voltage sags, two test cases are considered: (A) balanced grid voltage sags, and (B) unbalanced grid voltage sags.

4.1. Balanced grid voltage sags

In this test a balanced voltage sag occurs from $t = 0.2$ s to $t = 0.4$ s, the grid voltages are set to $V_g = 0.6$ pu during the faulty period, as shown in Fig. 7. The same test is performed for evaluating the selected adaptive observers in the LVRT application.

4.1.1. Global adaptive observer

Starting with GAO, the obtained results are summarized in Fig. 8. SYRF grid voltages are calculated through the GAO, followed by sequence separation through Eqs. (19) and (20). These voltages are plotted in Fig. 8(a), which shows that SYRF voltages converge within one grid cycle, i.e., 20 ms. The occurred fault requires a current exceeding the threshold value, which enables the current limiting process to ensure that the injected currents equal at most the threshold value, as depicted in Fig. 8(b).

Since the dual current controller in SYRF is adopted in this work, positive and negative sequence components of the measured currents are needed to be available. For this purpose, the GAO is also used, and the results are shown in Fig. 8(c). Within two cycles, steady-state values of direct and quadrature axis currents are obtained. Moreover, the injected currents are balanced without any negative sequence. In order to meet grid code requirements and support the grid during voltage sags, reactive power is injected according to Eq. (5) which corresponds to 0.8 pu Active power reference is reduced gradually due to the current limiting process as shown in Fig. 8(d).

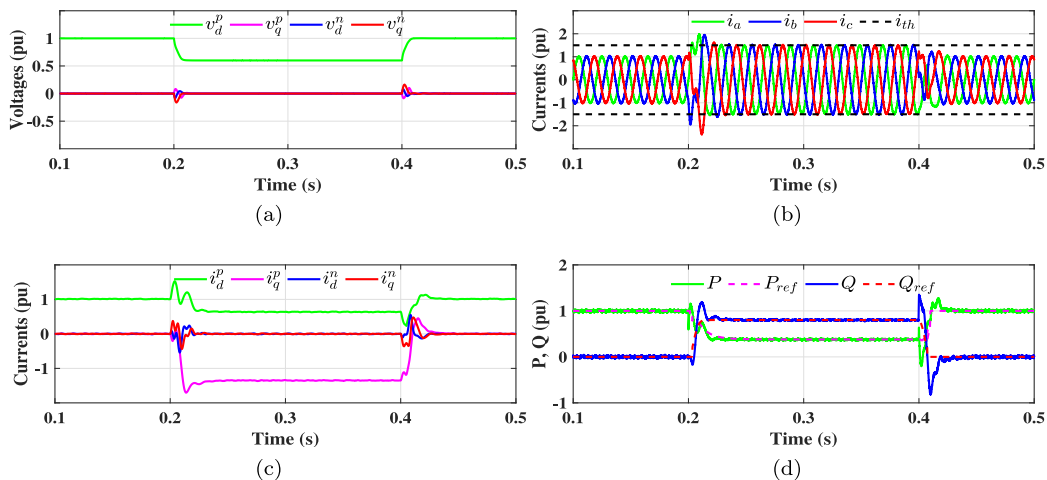


Fig. 8. LVRT under the balanced voltage sag test using GAO: (a) SYRF grid voltages, (b) Injected currents, (c) SYRF injected currents, and (d) Injected active and reactive powers.

4.1.2. Gain normalized adaptive observer

The same balanced fault is applied to evaluate the performance of GNAO. The obtained results using GNAO as the sequence estimators are given in Fig. 9. These results confirm the suitability of gain normalized adaptive observers in LVRT capability improvements, which are ensured with a fast convergence around two grid cycles. As shown in Fig. 9(a), the grid voltage sequences are obtained rapidly, with quick convergence to the steady-state values. The fast current limitation process during the grid fault period is clearly noticed in Fig. 9(b). Current sequences overshoot is improved by using the GNAO as depicted in Fig. 9(c). Grid code requirements are achieved by injecting the adequate powers as given in Fig. 9(d) according to the level of the balanced fault ($V_g = 0.6$ pu).

4.1.3. SOGI-type adaptive observer

In this case, SAO is considered as the voltages and currents sequence components separation method for the LVRT control purpose. The obtained results given in Fig. 10 show that this adaptive observer can provide a fast and accurate response under large magnitude balanced voltage sag. Stability enhancement performance is achieved using this observer, as evidenced by the voltage and current sequences presented in Figs. 10(a) and 10(c). All LVRT options are performed under this balanced fault, the injected currents are limited to avoid inverter damage, reactive power reference corresponds to the required value ($Q_{ref} = 0.8$ pu), and a reduced active power reference generated by the current limiting algorithm. These points are presented in Figs. 10(b) and 10(d).

4.2. Unbalanced grid voltage sags

In this case, an unbalanced voltage sag occurred from $t = 0.2$ s to $t = 0.4$ s. The asymmetrical fault is created by putting $v_b = 0.4$ pu and $v_c = 0.8$ pu as illustrated in Fig. 11. Therefore, during the faulty period, the grid voltage will be equal to $V_g = 0.73$ pu. The same simulation is carried out for evaluating the selected adaptive observers in the LVRT application.

4.2.1. Global adaptive observer

Simulation results under unbalanced voltage fault with GAO as the sequence estimators are given in Fig. 12. From the SYRF voltages in Fig. 12(a), it can be seen that negative sequence voltages appear during the faulty period due to the asymmetrical fault. The current limiter process is enabled under this fault to limit the injected currents at the threshold value as illustrated in Fig. 12(b). Despite the difference between per-phase current amplitudes, this limiter provides fast and accurate protection of the inverter and its semiconductor components.

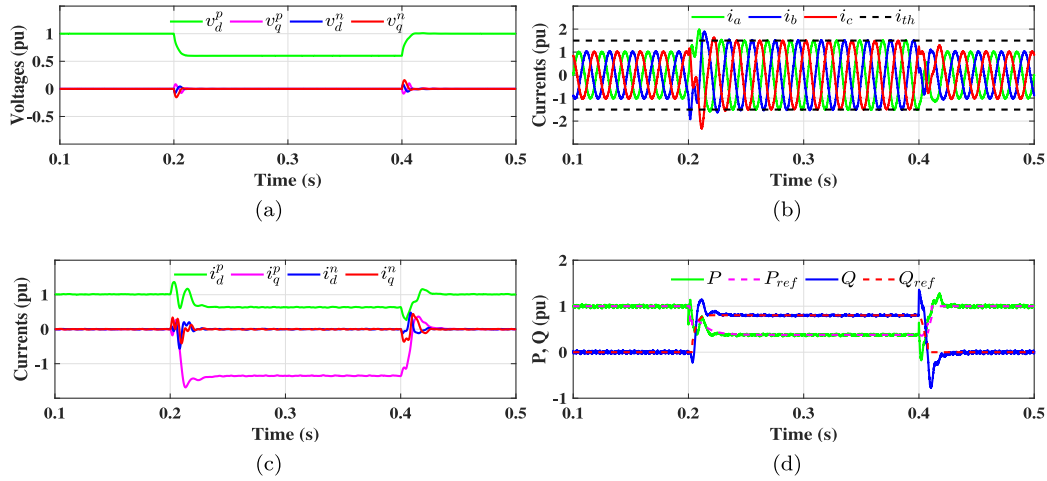


Fig. 9. LVRT under the balanced voltage sag test using GNAO: (a) SYRF grid voltages, (b) Injected currents, (c) SYRF injected currents, and (d) Injected active and reactive powers.

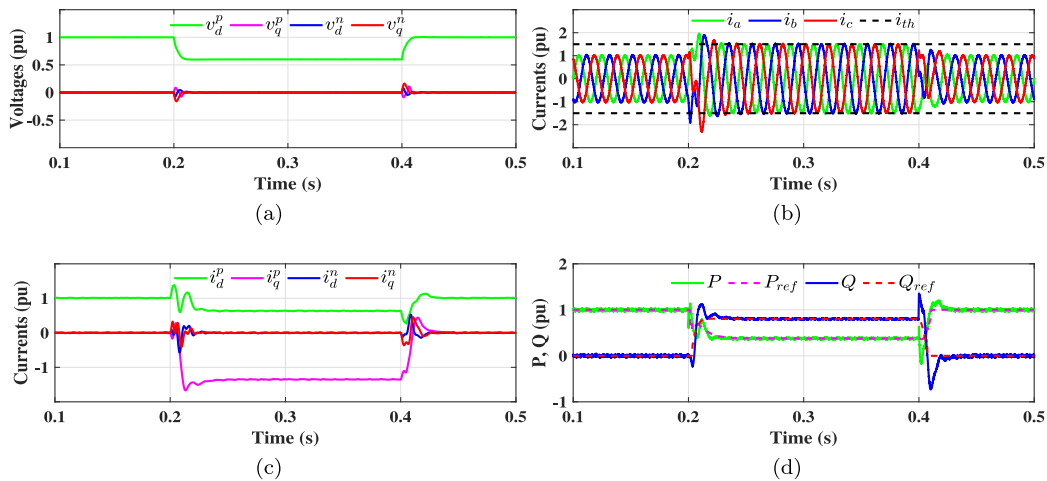


Fig. 10. LVRT under the balanced voltage sag test using SAO: (a) SYRF grid voltages, (b) Injected currents, (c) SYRF injected currents, and (d) Injected active and reactive powers.

The GAO is also used to obtain the current sequences, which are subsequently sent to the dual SYRF current controller. The current sequences are plotted in Fig. 12(c) which shows the negative sequence injection during the faulty period. The amount of this negative sequence is determined using Eq. (10) to deliver the required power references without active power oscillations. As shown in Fig. 12(d), the injected powers are in accordance with LVRT strategy requirements, i.e., reactive power of $Q_{ref} = 0.54$ pu is injected into the grid to support this voltage sag, the active power reference is reduced due to the current limiting process, and double-frequency oscillations exist only on the reactive power.

4.2.2. Gain normalized adaptive observer

Fig. 13 summarizes the obtained simulation results with GNAO as the estimator, which demonstrate the benefits of using this adaptive observer-based sequences extraction for LVRT capability application. The system steady-state is ensured after a delay of around two grid cycles. The grid voltage sequences including the negative ones are illustrated in Fig. 13(a) which are obtained during a very short duration under faulty conditions. The injected currents are sinusoidal, unbalanced, and limited to the threshold value, as shown in Fig. 13(b). The unbalanced currents are caused by the necessary negative sequence amount that must be injected into the grid to deal with the active power oscillations. This is illustrated in Fig. 13(c) which shows a clear overshoot in current sequences transition as seen also in GAO results.

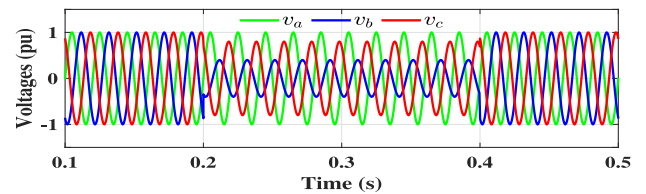


Fig. 11. Grid voltages during the unbalanced voltage sag test.

As shown in Fig. 13(d), injected powers correctly meet the grid code requirements mainly about the reactive power support ($Q_{ref} = 0.54$ pu) under voltage sags.

4.2.3. SOGI-type adaptive observer

To verify the effectiveness of the SAO under the same unbalanced fault, the voltage/current sequences are estimated by using the SAO. Fig. 14 gives the obtained results, which confirm the benefits of using adaptive observers-based sequences extractor in GCCs control. Smooth transition and stable performance are demonstrated in SYRF voltages and currents, as represented in Figs. 14(a) and 14(c), respectively. Unbalanced and limited currents are injected into the grid to deal with the active power oscillations, and also to meet the grid codes

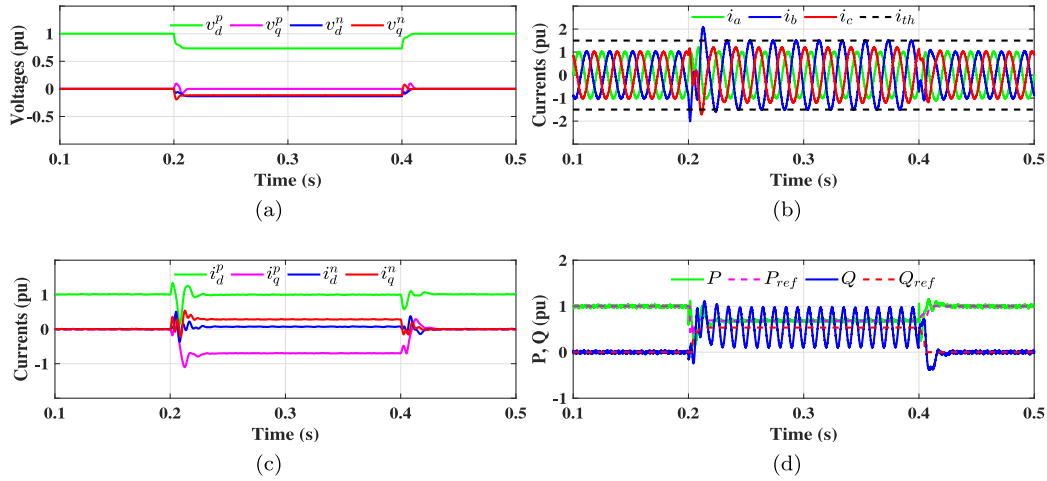


Fig. 12. LVRT under the unbalanced voltage sag test using GAO: (a) SYRF grid voltages, (b) Injected currents, (c) SYRF injected currents, and (d) Injected active and reactive powers.

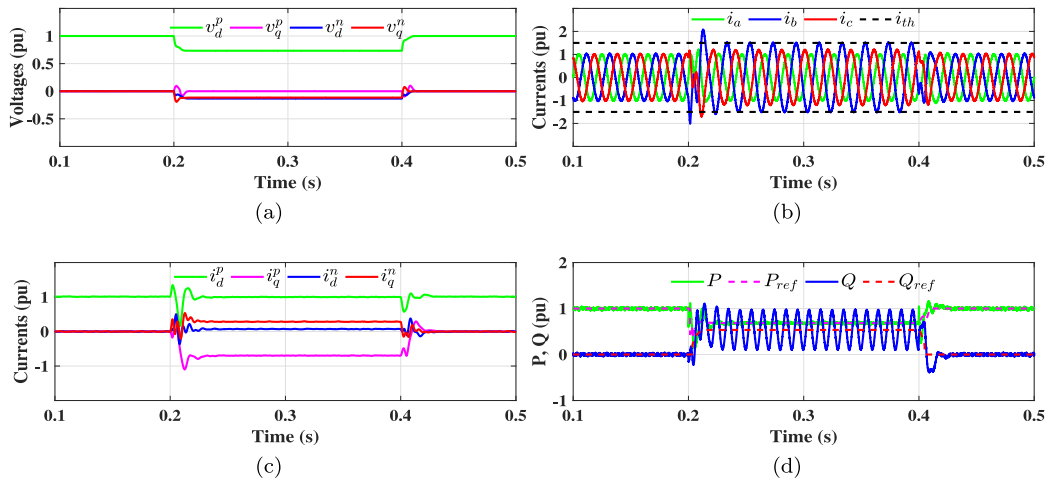


Fig. 13. LVRT under the unbalanced voltage sag test using GNAO: (a) SYRF grid voltages, (b) Injected currents, (c) SYRF injected currents, and (d) Injected active and reactive powers.

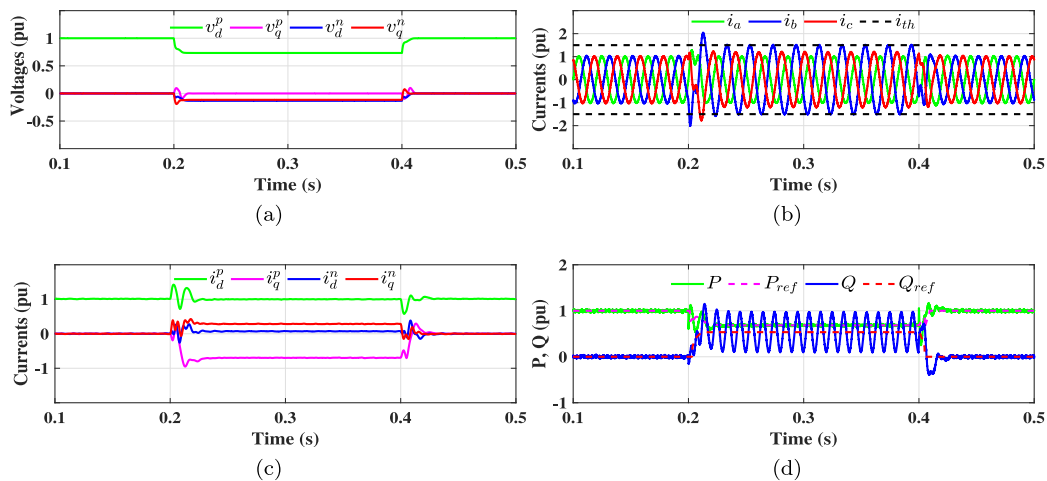


Fig. 14. LVRT under the unbalanced voltage sag test using SAO: (a) SYRF grid voltages, (b) Injected currents, (c) SYRF injected currents, and (d) Injected active and reactive powers.

requirements by ensuring the suitable reactive power reference under this grid voltage fault, as shown in Figs. 14(b) and 14(d), respectively.

In order to compare these adaptive observers in terms of grid frequency estimation, another simulation is carried out. Since the grid

Table 2
Injected currents THD during line inductor variation.

Observer	Line inductor		
	1.25L	L	0.75L
SAO	1.61%	1.96%	2.51%
GAO	1.91%	2.05%	2.50%
GNAO	1.94%	2.00%	2.60%

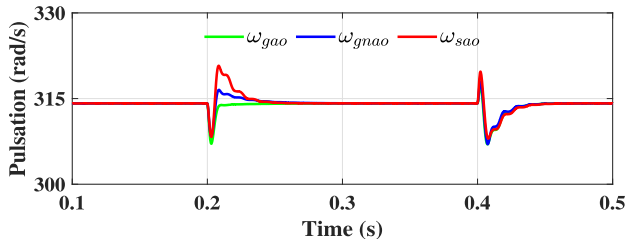


Fig. 15. Estimated grid frequency under voltage sag of 0.6 pu.

frequency update law is attached to the phase “a” voltage, a test of voltage sag of 0.6 pu in this phase is performed. The obtained result is given in Fig. 15. It is interesting to notice the rapidity of all studied observers in frequency estimation. The delay to get the steady-state is approximated at around two grid cycles for the three observers, which confirms the tuning procedure for the observer gains. As discussed above, SAO and GNAO are less sensitive to the voltage sags compared to GAO, as shown at $t = 0.2$ s when the fault occurred. This is demonstrated by the small overshoot in SAO and GNAO compared to GAO.

4.3. Control performance in the presence of parameter uncertainties

Due to aging and change in operational conditions, parameter uncertainties are often common in practice. In the case of VSI, the filter inductor value may change due to over-loading-related thermal stress, operating temperature, etc. Similarly, grid impedance may vary due to changes in the power generation/load pattern. These unforeseen events can manifest as an increase or decrease in the line inductor value, thereby directly influencing the performance of the current controller, potentially leading to instability if the controller’s sensitivity has not been studied.

The effectiveness of the control structure shown in Fig. 4 is re-evaluated under an unbalanced situation, while also simulating a notable variation in the filter inductor. Two simulation studies have been

considered with $\pm 25\%$ variation from the nominal case while testing all adaptive observers.

As illustrated in Fig. 16, the designed control structure is able to operate even under decreased inductor filter. By using the three adaptive observers in the current control, no signs of instability are detected throughout the entire process, even when faced with an unbalanced fault, the system remains unfazed and continues to ensure LVRT capability seamlessly.

Similarly, Fig. 17 demonstrates the impact of increasing the filter inductor on the injected currents. An interesting observation is that the controller’s sensitivity remains practically unaffected by the notable 25% increase. This remarkable finding underscores the robustness and reliability of the controller against parametric uncertainties.

Harmonic distortion level of the line currents is also computed to highlight the filter inductor variation effect on the THD of currents. As shown in Table 2, the THD of currents is generally within acceptable limits for the different inductance values. Moreover, the three adaptive observers have demonstrated their suitability in facilitating grid-connecting inverters under asymmetric conditions. Additionally, it is noteworthy that higher inductance results in better injected current quality, albeit at the cost of increased response time due to the corresponding increase in the time constant.

In addition to the simulation studies presented here, interested readers may consult [71] for an analytical sensitivity analysis of the control subject to parametric uncertainties.

5. Experimental results

For the experimental validation, a laboratory platform based on a two-level voltage source inverter equipped with an RL filter is built. The same system parameters are also used for the practical implementation, as listed in Table 1. Fig. 18 shows the considered laboratory test setup, which is composed of a step-down grid transformer ensuring a low grid voltage level, two single-phase autotransformers to create asymmetrical voltage faults, a real-time control board based on dSPACE associated with MATLAB/Simulink, and measurement equipment including grid voltage and injected current sensors with an oscilloscope and a real-time screen.

In order to be consistent with the simulation tests, both balanced and unbalanced voltage sags are studied in practice while using the adaptive observers as discussed above.

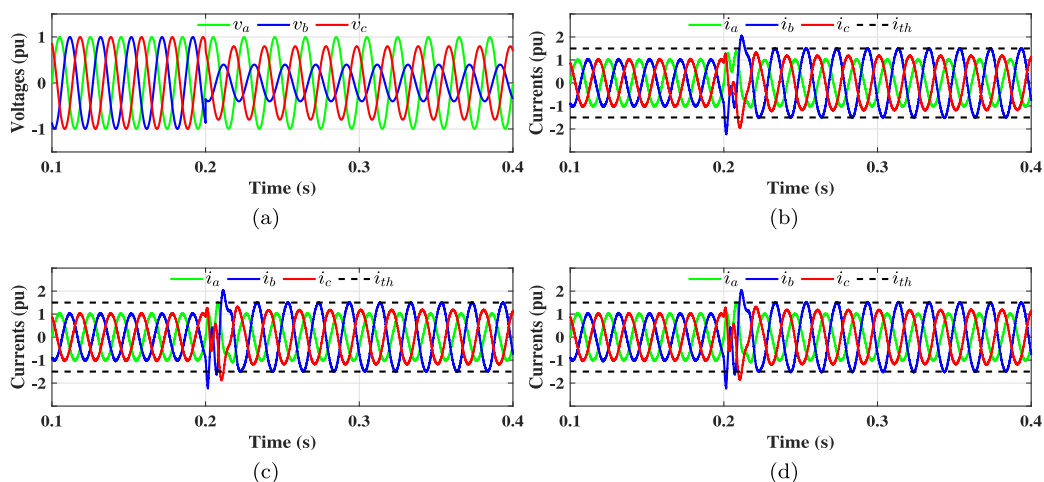


Fig. 16. Grid voltages and currents during unbalanced situation and -25% of filter inductor: (a) Grid voltages, (b) Injected currents using SAO, (c) Injected currents using GAO, and (d) Injected currents using GNAO.

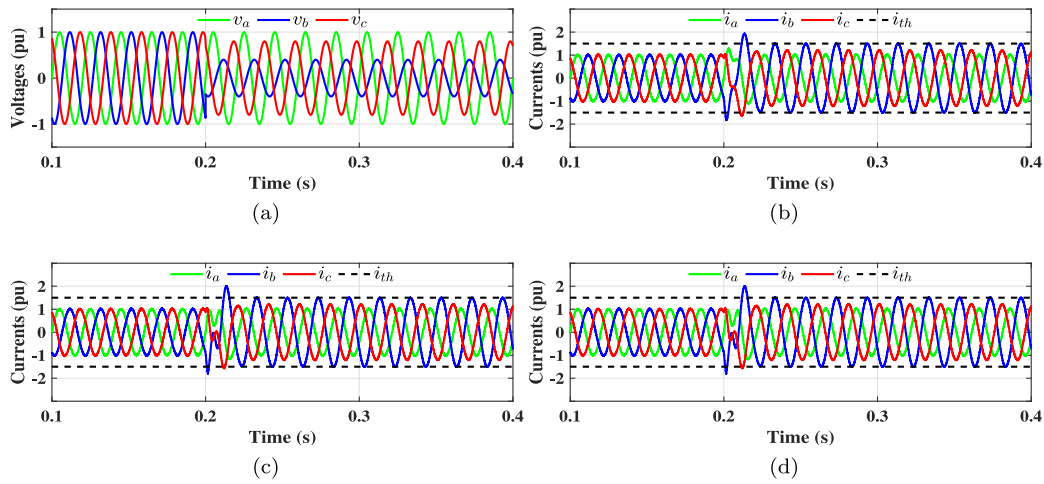


Fig. 17. Grid voltages and currents during unbalanced situation and +25% of filter inductor: (a) Grid voltages, (b) Injected currents using SAO, (c) Injected currents using GAO, and (d) Injected currents using GNAO.

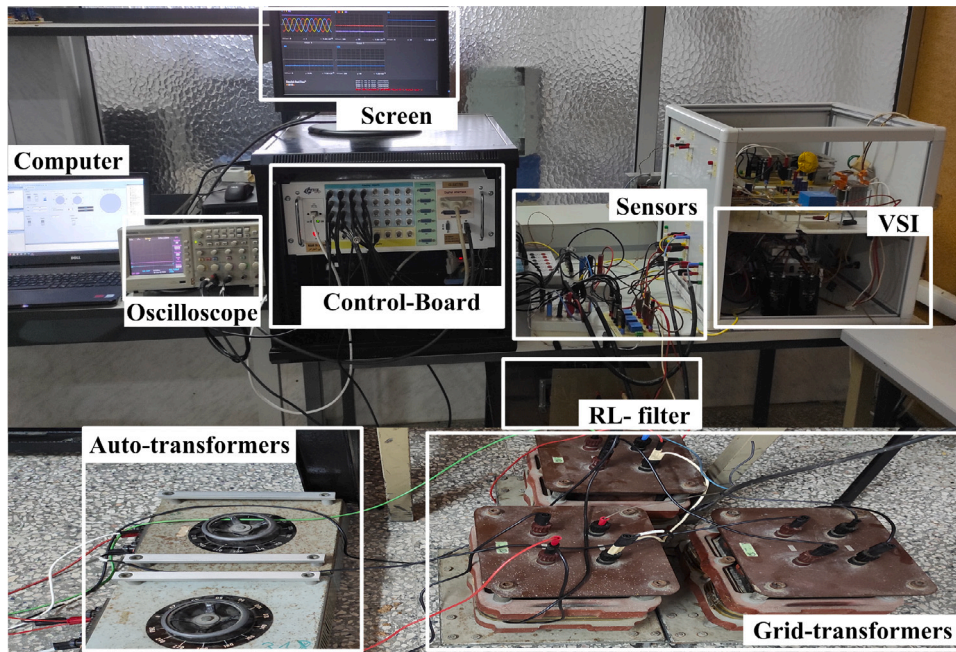


Fig. 18. Experimental test setup.

5.1. Balanced grid voltage sags

A symmetrical voltage sag occurs from $t = 40$ s to $t = 60$ s. The grid voltages are equal to $V_g = 0.6$ pu during the faulty conditions, as depicted in Fig. 19. This fault is maintained in order to evaluate each adaptive observer and show its performance under an abrupt balanced voltage sag.

5.1.1. Global adaptive observer

As can be seen in Fig. 20, the obtained results confirm the suitability of GAO as sequence estimators for LVRT applications. Grid voltages in SYRF are estimated rapidly and accurately as shown in Fig. 20(a). Since the voltage fault is balanced, the negative sequence is estimated as zero during the faulty interval. If any current limiter process is employed in this case, the injected currents exceed the threshold value and can damage the inverter. However, the effectiveness of the used current limiter is clearly proven in Fig. 20(b), which ensures a safe operation of the inverter with a very small transient period.

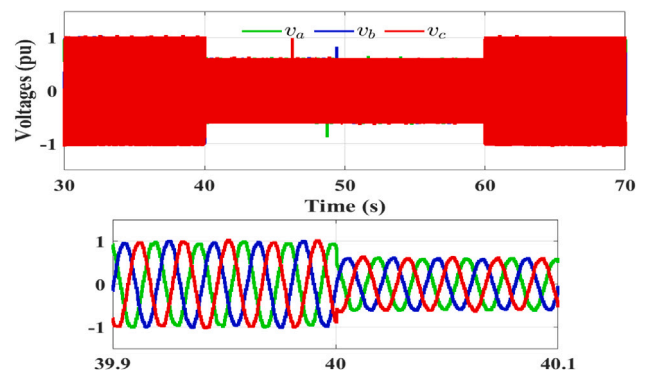


Fig. 19. Grid voltages during the balanced voltage sag test.

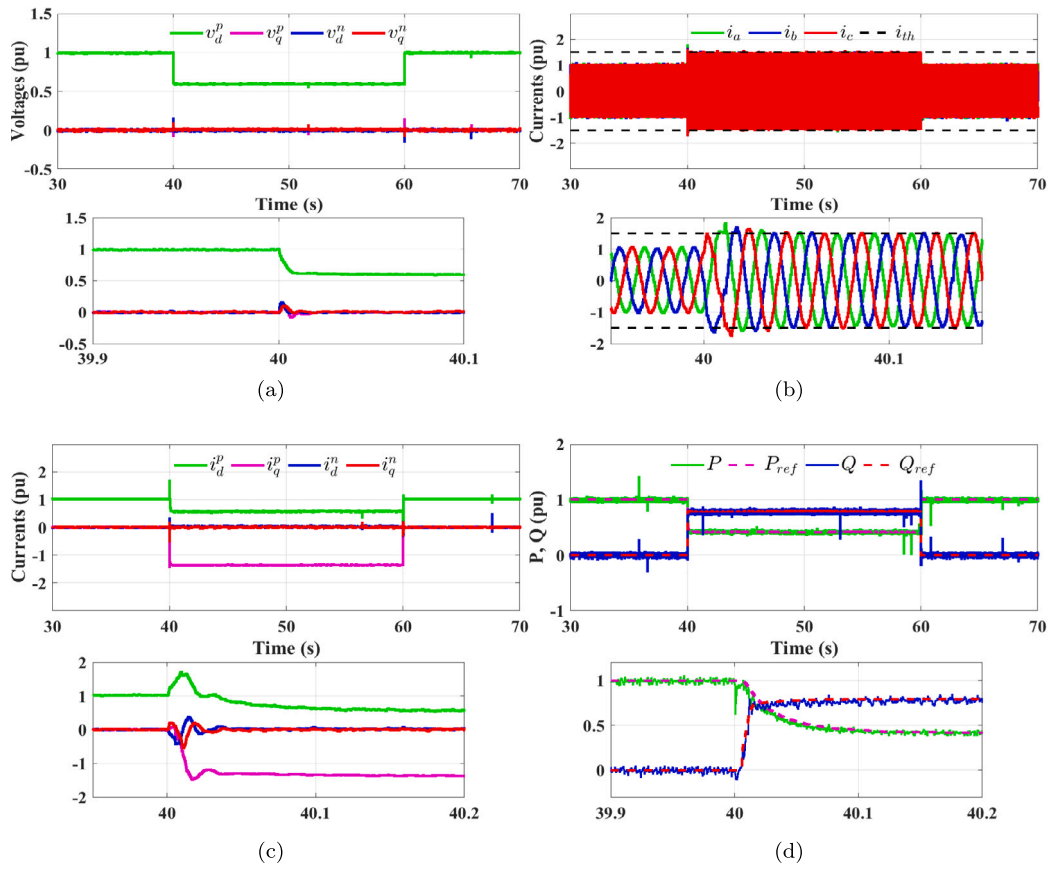


Fig. 20. Experimental LVRT under the balanced voltage sag test using GAO: (a) SYRF grid voltages, (b) Injected currents, (c) SYRF injected currents, and (d) Injected active and reactive powers.

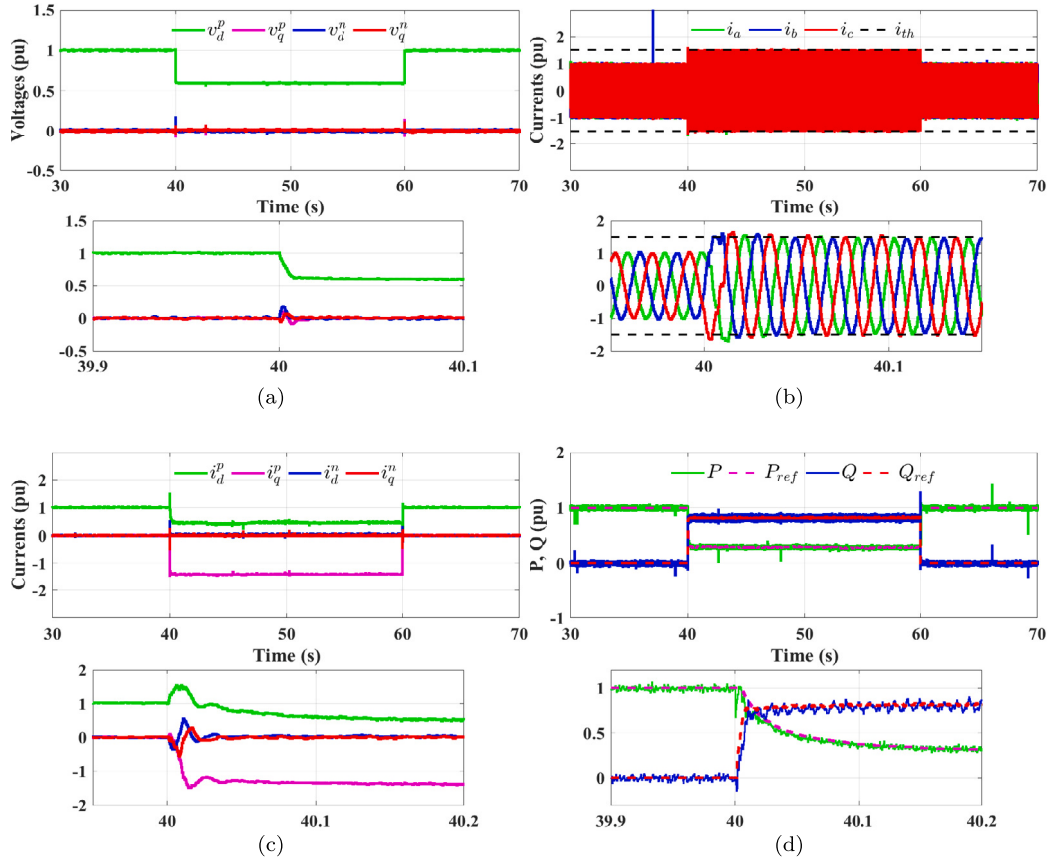


Fig. 21. Experimental LVRT under the balanced voltage sag test using GNAO: (a) SYRF grid voltages, (b) Injected currents, (c) SYRF injected currents, and (d) Injected active and reactive powers.

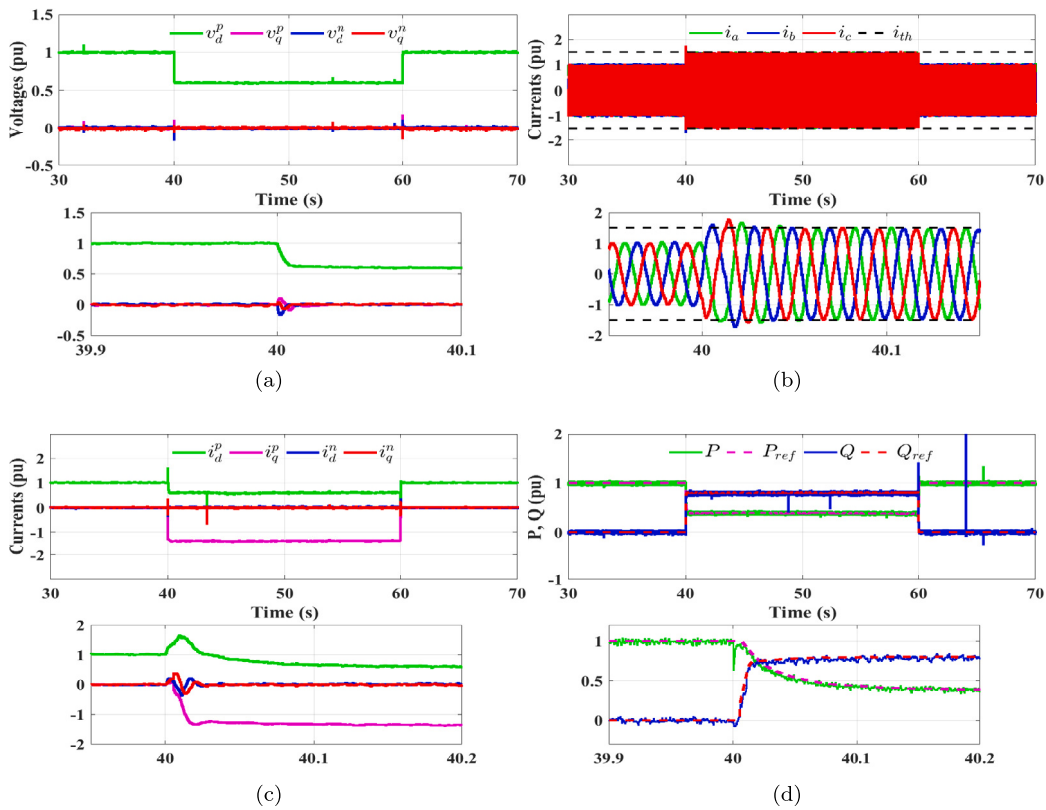


Fig. 22. Experimental LVRT under the balanced voltage sag test using SAO: (a) SYRF grid voltages, (b) Injected currents, (c) SYRF injected currents, and (d) Injected active and reactive powers.

Injected currents in SYRF are represented in Fig. 20(c). In order to meet grid code requirements, the exact reactive power amount must be injected according to the voltage fault level. As depicted in Fig. 20(d), the reactive power reference is modified from zero to $Q_{ref} = 0.8$ pu which corresponds exactly to 0.4 pu of grid voltage sag. Due to the current limiting process, active power reference is reduced gradually to maintain the injected currents at most equal to the threshold value.

5.1.2. Gain normalized adaptive observer

The obtained results with GNAO-based sequence components estimators are represented in Fig. 21. Due to the fault appearance at $t = 40$ s, LVRT options are ensured after a short transient period for the system recovery. Grid voltages in SYRF converged rapidly to steady-state values, as seen in Fig. 21(a). Injected currents are well limited to avoid any over-current inverter damage as shown in Fig. 21(b). Current sequences as plotted in 21(c) are also estimated using GNAO which allows a better estimation under the presence of balanced voltage sags. Fig. 21(d) shows the injected powers during the experiment. Some reactive power is injected into the grid as per grid codes to support the grid voltage sags. In addition, active power reference is reduced due to the current limiting process. As can be seen in Fig. 21(d) that the injected powers have a little more high-frequency fluctuations compared with those using GAO.

5.1.3. SOGI-type adaptive observer

The obtained experimental results using SAO are summarized in Fig. 22. The suitability of this estimator to improve LVRT capability is clearly reflected in the obtained results. Enhanced stability and short settling time are achieved in voltage and current sequences separation by using this adaptive observer, as can be seen in Figs. 22(a) and 22(c), respectively. Injected currents are sinusoidal and limited during the faulty conditions to protect the inverter from over-current damage, as shown in Fig. 22(b). Grid code requirements are ensured by injecting

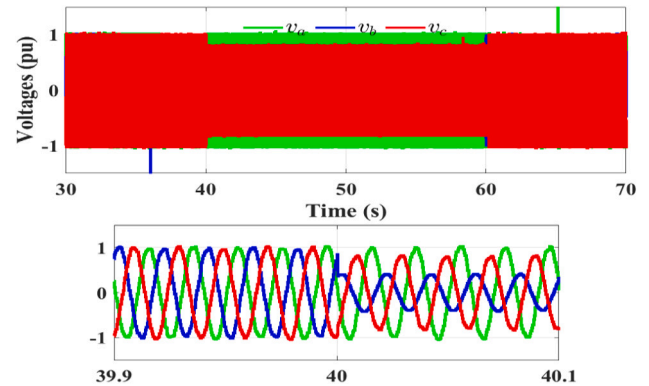


Fig. 23. Grid voltages during the unbalanced voltage sag test.

the exact value of reactive power according to the voltage fault level. This observer is much better in terms of high-frequency power fluctuations compared with those using GAO or GNAO. Moreover, the settling time in power convergence is improved using SAO. These points are clearly noticed in Fig. 22(d).

5.2. Unbalanced grid voltage sags

In order to experimentally validate the selected observer under unbalanced voltage sag, extensive experiments are carried out. An unbalanced voltage sag occurs from $t = 40$ s to $t = 60$ s by putting $v_b = 0.4$ pu and $v_c = 0.8$ pu as illustrated in Fig. 23. Therefore, the grid voltage will be equal to $V_g = 0.73$ pu during the faulty period. This fault is maintained to evaluate the selected adaptive observers at the same conditions while ensuring LVRT objectives.

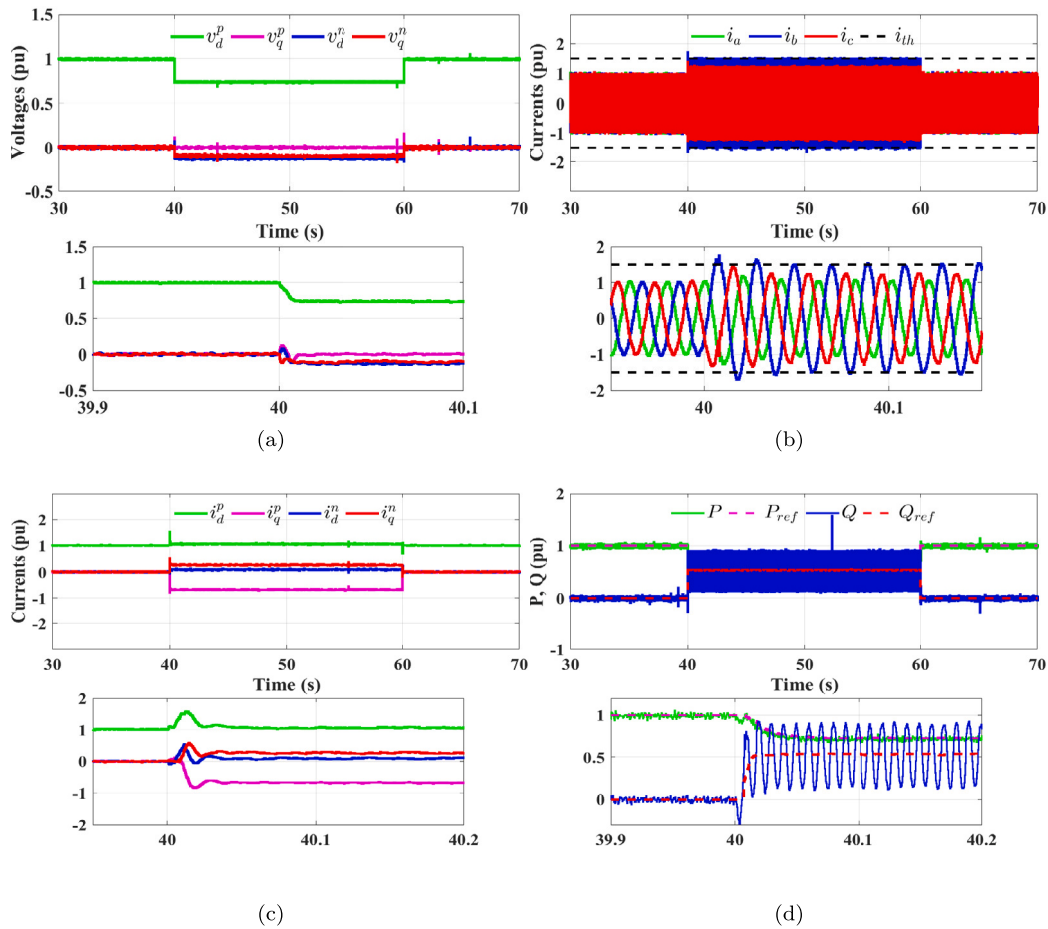


Fig. 24. Experimental LVRT under the unbalanced voltage sag test using GAO: (a) SYRF grid voltages, (b) Injected currents, (c) SYRF injected currents, and (d) Injected active and reactive powers.

5.2.1. Global adaptive observer

The obtained results are provided in Fig. 24. The SYRF grid voltages are estimated firstly by GAO in natural reference frame via Eqs. (19) and (20). These voltages are then transformed into SYRF with the help of the $abc-dq$ transform. As shown in Fig. 24(a), the voltage sequences are available during the entire experiment duration even under the unbalanced fault. The negative sequence also exists in the direct and quadrature axis due to the type of fault. The chosen current limiter shows its performance in terms of rapidity and stability, as can be noticed in Fig. 24(b). The injected currents are unbalanced, sinusoidal, and well-limited at the threshold value during the fault period. This is achieved with sub-two-cycle convergence time.

The current sequences are obtained in the same way as the voltage ones. These current sequences are required for controlling the GCCs under faulty conditions, i.e., in presence of both positive and negative sequence currents. As illustrated in Fig. 24(c), negative sequence currents are injected into the grid for active power oscillations elimination under asymmetrical fault. The injected powers are plotted in Fig. 24(d) which shows very good compliance to grid codes requirements under this voltage fault level, i.e., $Q_{ref} = 0.54$ pu is injected to support a voltage sag of 0.27 pu. Moreover, no active power oscillations confirm the exact values of the injected negative currents into the grid.

5.2.2. Gain normalized adaptive observer

Fig. 25 details the obtained experimental results under asymmetrical voltage sags using GNAO. The grid voltage sequences are represented in Fig. 25(a) which show a good performance in terms of rapidity and robustness even under unbalanced faults. The negative-sequence voltages are estimated perfectly to give an accurate fault

quantification. The current limiter is enabled to avoid inverter damage by ensuring the injected currents equal at most the threshold value even with the difference in per-phase amplitudes, as illustrated in Fig. 25(b). The settling time for current sequences estimation is improved by using GNAO with a little overshoot compared to the previous observer, i.e., GAO. This result is represented in Fig. 25(c). All LVRT ancillary services are achieved in this experiment as shown in Fig. 25(d) by injecting the suitable reactive power to support the grid during voltage sag, suppressing active power oscillations during the fault, and decreasing active power reference due to the current limiting process.

5.2.3. SOGI-type adaptive observer

The obtained experimental results using SAO-based sequence components estimators are given in Fig. 26. The benefits of using an adaptive observer in GCCs control scheme are clearly visible. Improved performance is offered by using SAO compared to the other estimators such as short settling time, smooth transition at fault appearance, and more stability in the estimated sequences. These points are demonstrated in Figs. 26(a) and 26(c), which give grid voltage and injected current sequences, respectively. The achieved advantages using SAO allow the fast response of the current limiting algorithm and improved injected powers according to the grid code exigences with negligible high-frequency fluctuations. The injected currents in the natural reference frame and powers are plotted in Figs. 26(b) and 26(d), respectively.

In order to verify each adaptive observer and show its performance in terms of grid frequency estimation, an experimental test is carried out. Same to the simulation scenario explained in Fig. 15, the fault is created in phase “a” voltage, which is responsible for the frequency

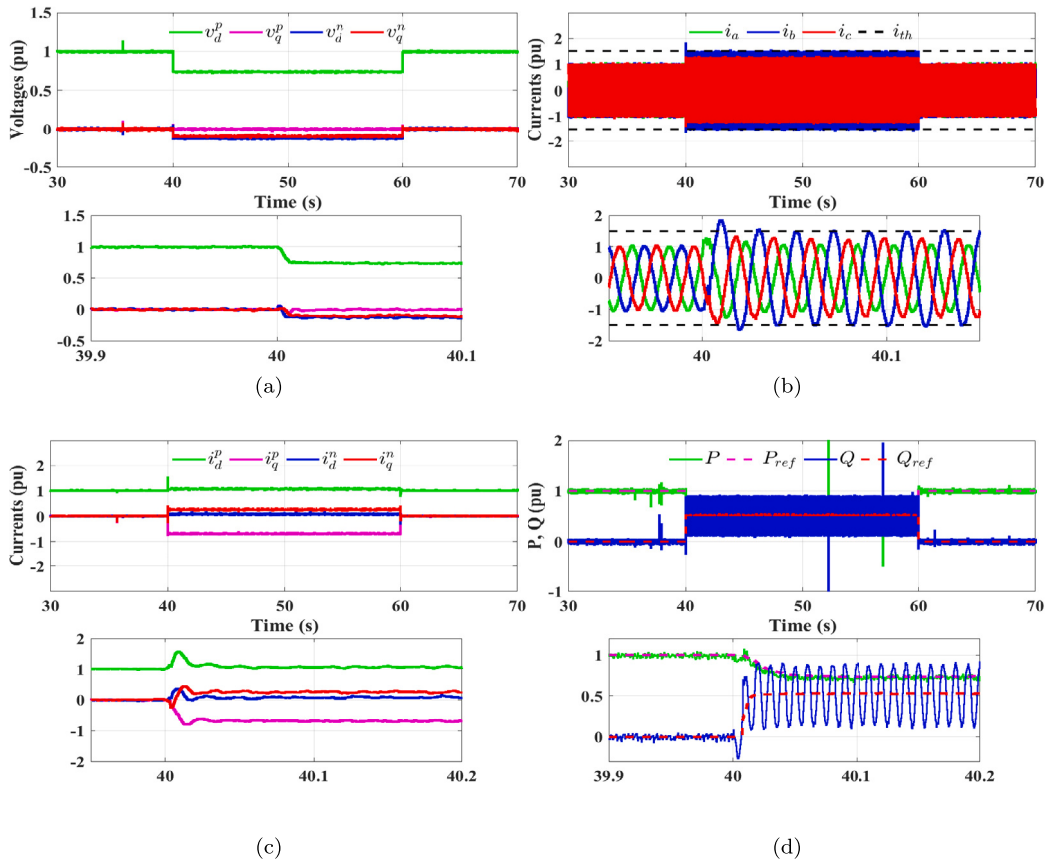


Fig. 25. Experimental LVRT under the unbalanced voltage sag test using GNAO: (a) SYRF grid voltages, (b) Injected currents, (c) SYRF injected currents, and (d) Injected active and reactive powers.

update law. As can be seen in Fig. 27, the grid frequency is estimated even in presence of grid voltage sags. This result confirms also the less sensitivity of SAO and GNAO to the voltage sags, which have a small overshoot at $t = 40$ s. Since SAO has negligible high-frequency ripples, it is judged as the best observer in frequency estimation for grid-synchronization purposes.

By carefully observing all the simulation and experimental results, it can be seen that the experimental results demonstrate a high degree of congruence with the simulated results. This validates the results developed in this work.

6. Discussions

The achieved results highlight the remarkable suitability of adaptive observers in enhancing the control of GCCs, particularly when confronted with grid voltage disturbances. By accurately estimating voltage and current sequences, the adaptive observers contribute significantly to the improved performance of GCCs, enabling them to maintain stable and accurate operation in adverse grid conditions.

The efficiency of the employed techniques becomes readily apparent through various experimental results, showcasing a superior real-time response in comparison to relatively medium computational complexity. Moreover, the desired objectives of LVRT applications are achieved in all simulations or experiments demonstrating how the observers effectively estimate voltage/current sequences, react to grid disturbances, calculate the desired active and reactive powers, and provide accurate control signals.

The accuracy of the implemented observers is thoroughly assessed through experimental evaluation, with a focus on tracking the desired reactive power. The results demonstrate a notable distinction in accuracy performance among the different observer types. Specifically,

Table 3
Comparative analysis of the adaptive observers-based LVRT control.

Features	SAO	GAO	GNAO
Dynamic response	Very fast	Very fast	Very fast
Voltage sag sensitivity	Low	High	Low
Computational complexity	Medium	Medium	High
Harmonics sensitivity	Low	Medium	Medium
Accuracy	High	Medium	Medium

when using the SAO, an impressive accuracy level of approximately 95% is achieved under balanced voltage sags. On the other hand, when employing the GAO or GNAO, the reactive power tracking accuracy is observed to be around 87%. These findings highlight the superior accuracy attained by SAO in comparison to the alternative observer methods, underscoring its efficacy in accurately tracking the desired reactive power in the presence of balanced voltage sags. All discussed results are summarized in Table 3.

Based on the results illustrated in Table 3, one can find that SAO-based controllers achieved better results in terms of convergence time, sensitivity to harmonics, accuracy, etc. compared to GAO and GNAO. This finding can be useful to readers and industrial practitioners in selecting the right sequence estimation methods for LVRT control of grid-connected converter-based renewable energy sources.

7. Conclusion

A comparative study of three adaptive observers-based sequence separation methods is performed in this paper. To ensure a fair comparison between the observers, a systematic gain-tuning procedure has been followed using the settling-time criterion. Despite being fairly

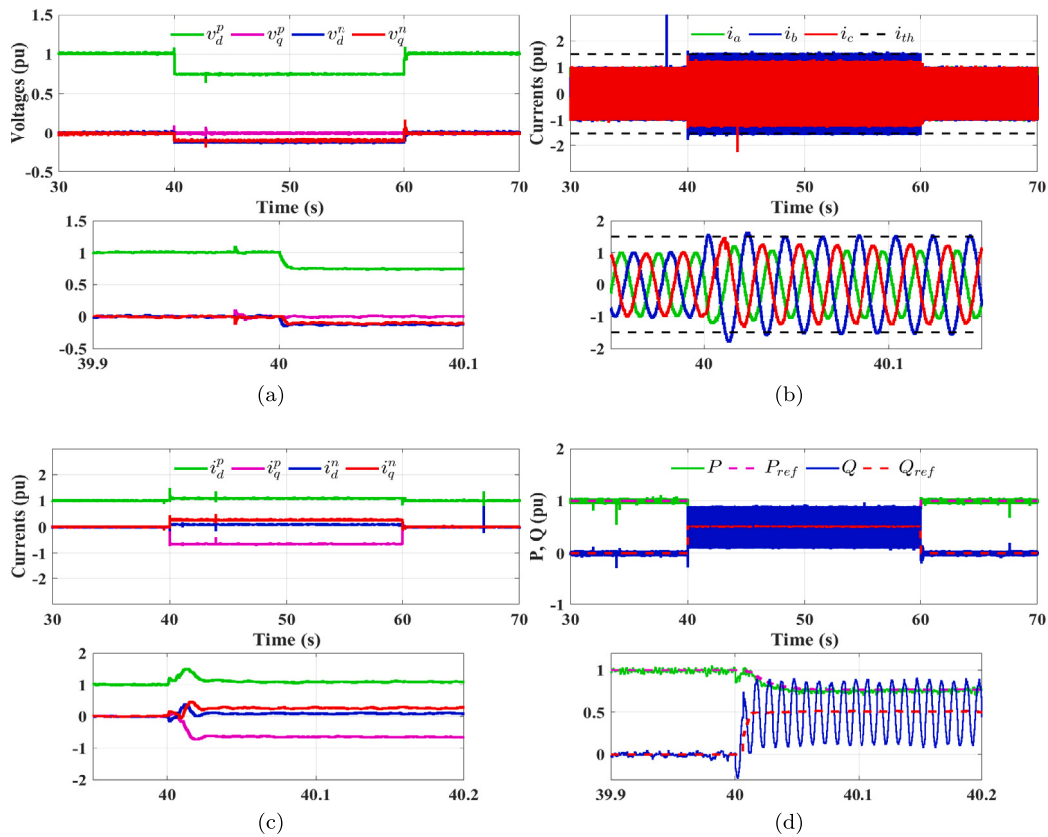


Fig. 26. Experimental LVRT under the unbalanced voltage sag test using SAO: (a) SYRF grid voltages, (b) Injected currents, (c) SYRF injected currents, and (d) Injected active and reactive powers.

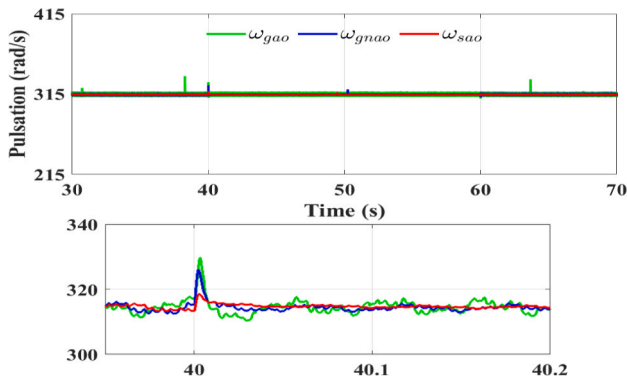


Fig. 27. Experimental test to estimate grid frequency under voltage sag of 0.6 pu.

tuned, these observers have their own merits and demerits in terms of dynamic response, voltage sag and harmonics sensitivity, computational complexity, and accuracy. The selected observers prove their suitability for LVRT capability enhancement under balanced and unbalanced grid faults. The proposed control strategy ensures all LVRT ancillary services while embedding the adaptive observers for grid-synchronization issues. Required reactive power is injected into the grid according to GCs requirements to improve grid stability under voltage sags, avoid converter over-current related tripping by limiting the injected currents using an online active power reducing approach, estimate the positive and negative sequences of the grid voltage and currents and obtain their angular frequency through the studied adaptive observers, suppress active power oscillation under asymmetrical

faults by calculating new current references in SYRF, and via the adaptive observers, the actual currents sequences are regulated separately to follow these new references.

Simulation results of all observers clearly highlight the effectiveness and suitability of the studied adaptive observers within LVRT control under symmetrical/asymmetrical faults. A laboratory-scale setup is considered, which is composed of an inductive filtered grid-connected inverter and dSPACE real-time control board to benchmark the proposed control strategy including the adaptive observers comparative study. Obtained results are in accordance with simulation ones and confirm also the flexibility and rapidity obtained by using adaptive observers-based grid-synchronizing sequence extraction strategies in LVRT control architecture. In addition, qualitative performance comparisons between the observers are presented, which will guide practitioners to select the right observer for their LVRT controller development for GCC application.

CRediT authorship contribution statement

Fayçal Benyamina: Conceptualization, Methodology, Simulations, Data analysis, Writing – original draft. **Hafiz Ahmed:** Conceptualization, Methodology, Data analysis, Reviewing and editing. **Abdeldjabar Benrabah:** Data analysis, Writing – review & editing. **Farid Khoucha:** Data analysis, Writing – review & editing. **Yahia Achour:** Reviewing and editing. **Mohamed Benbouzid:** Methodology, Data analysis, Supervision, Writing – review & editing.

Declaration of competing interest

The authors declare that they have no known competing financial interests or personal relationships that could have appeared to influence the work reported in this paper.

Data availability

No data was used for the research described in the article.

Acknowledgments

The work of H. Ahmed is partially supported by the Sêr Cymru programme by Welsh European Funding Office (WEFO) under the European Regional Development Fund (ERDF) through Bangor University. This work was supported in part by the Royal Society, United Kingdom under grant RGS\R2\192245.

References

- [1] Blaabjerg F, Teodorescu R, Liserre M, Timbus AV. Overview of control and grid synchronization for distributed power generation systems. *IEEE Trans Ind Electron* 2006;53(5):1398–409.
- [2] Zia MF, Elbouchikhi E, Benbouzid M. Microgrids energy management systems: A critical review on methods, solutions, and prospects. *Appl Energy* 2018;222:1033–55.
- [3] Hosenuzzaman M, Rahim N, Selvaraj J, Hasanuzzaman M, Malek A, Nahar A. Global prospects, progress, policies, and environmental impact of solar photovoltaic power generation. *Renew Sustain Energy Rev* 2015;41:284–97.
- [4] Keirstead J, Jennings M, Sivakumar A. A review of urban energy system models: Approaches, challenges and opportunities. *Renew Sustain Energy Rev* 2012;16(6):3847–66.
- [5] Tawalbeh M, Al-Othman A, Kafiah F, Abdelsalam E, Almomani F, Alkasrawi M. Environmental impacts of solar photovoltaic systems: A critical review of recent progress and future outlook. *Sci Total Environ* 2021;759:143528.
- [6] Kahwash F, Maheri A, Mahkamov K. Integration and optimisation of high-penetration Hybrid Renewable Energy Systems for fulfilling electrical and thermal demand for off-grid communities. *Energy Convers Manage* 2021;236:114035.
- [7] Zia MF, Benbouzid M, Elbouchikhi E, Muyeen S, Techato K, Guerrero JM. Microgrid transactive energy: Review, architectures, distributed ledger technologies, and market analysis. *IEEE Access* 2020;8:19410–32.
- [8] Al-Shetwi AQ, Hannan M, Jern KP, Mansur M, Mahlia T. Grid-connected renewable energy sources: Review of the recent integration requirements and control methods. *J Clean Prod* 2020;253:119831.
- [9] Chandra A, Singh G, Pant V. Protection of AC microgrid integrated with renewable energy sources—A research review and future trends. *Electr Power Syst Res* 2021;193:107036.
- [10] Li Z, Hu J, Chan KW. A new current limiting and overload protection scheme for distributed inverters in microgrids under grid faults. *IEEE Trans Ind Appl* 2021;57(6):6362–74.
- [11] Argyrou MC, Marouchos CC, Kalogirou SA, Christodoulides P. A novel power management algorithm for a residential grid-connected PV system with battery-supercapacitor storage for increased self-consumption and self-sufficiency. *Energy Convers Manage* 2021;246:114671.
- [12] Shair J, Li H, Hu J, Xie X. Power system stability issues, classifications and research prospects in the context of high-penetration of renewables and power electronics. *Renew Sustain Energy Rev* 2021;145:111111.
- [13] Khan A, Hosseinzadehtaher M, Shadmand MB, Bayhan S, Abu-Rub H. On the stability of the power electronics-dominated grid: A new energy paradigm. *IEEE Ind Electron Mag* 2020;14(4):65–78.
- [14] Meegahapola L, Sguarezi A, Bryant JS, Gu M, Conde D ER, Cunha R, et al. Power system stability with power-electronic converter interfaced renewable power generation: Present issues and future trends. *Energies* 2020;13(13):3441.
- [15] Khalid A, Stevenson A, Sarwat AI. Overview of technical specifications for grid-connected microgrid battery energy storage systems. *IEEE Access* 2021;9:163554–93.
- [16] Grid Code, High and extra high voltage. Bayreut, Germany: E.ON-Netz GmbH; 2006, 2006. URL <http://www.eon-netz.com/>.
- [17] Anzalchi A, Sarwat A. Overview of technical specifications for grid-connected photovoltaic systems. *Energy Convers Manage* 2017;152:312–27.
- [18] Teodorescu R, Liserre M, Rodriguez P. Grid requirements for PV. In: *Grid converters for photovoltaic and wind power systems*. John Wiley & Sons, Ltd; 2010, p. 31–42. <http://dx.doi.org/10.1002/9780470667057.ch3>.
- [19] Yang Y, Enjeti P, Blaabjerg F, Wang H. Suggested grid code modifications to ensure wide-scale adoption of photovoltaic energy in distributed power generation systems. In: 2013 IEEE industry applications society annual meeting. IEEE; 2013, p. 1–8.
- [20] Khan H, Chacko SJ, Fernandes BG, Kulkarni A. Reliable and effective ride-through controller operation for smart PV systems connected to LV distribution grid under abnormal voltages. *IEEE J Emerg Sel Top Power Electron* 2019;8(3):2371–84.
- [21] Çelik D, Meral ME. Voltage support control strategy of grid-connected inverter system under unbalanced grid faults to meet fault ride through requirements. *IET Gener Transm Distrib* 2020;14(16):3198–210.
- [22] Benyamina F, Benrabah A, Khoucha F, Benbouzid M. An improved control strategy for grid-tied inverters under faulty grid conditions. In: *Artificial intelligence and heuristics for smart energy efficiency in smart cities*. Springer International Publishing; 2021, p. 342–52. http://dx.doi.org/10.1007/978-3-030-92038-8_35.
- [23] Huka GB, Li W, Chao P, Peng S. A comprehensive LVRT strategy of two-stage photovoltaic systems under balanced and unbalanced faults. *Int J Electr Power Energy Syst* 2018;103:288–301.
- [24] Jaalam N, Rahim N, Bakar A, Tan C, Haidar AM. A comprehensive review of synchronization methods for grid-connected converters of renewable energy source. *Renew Sustain Energy Rev* 2016;59:1471–81.
- [25] Mohammadi J, Afsharnia S, Vaez-Zadeh S. Efficient fault-ride-through control strategy of DFIG-based wind turbines during the grid faults. *Energy Convers Manage* 2014;78:88–95.
- [26] Wen H, Fazeli M. A low-voltage ride-through strategy using mixed potential function for three-phase grid-connected PV systems. *Electr Power Syst Res* 2019;173:271–80.
- [27] Meral ME, Çelik D. A comprehensive survey on control strategies of distributed generation power systems under normal and abnormal conditions. *Annu Rev Control* 2019;47:112–32.
- [28] Ahmed H, Benbouzid M. Adaptive observer-based grid-synchronization and sequence extraction techniques for renewable energy systems: A comparative analysis. *Appl Sci* 2021;11(2):653.
- [29] Meral ME, Çelik D. Mitigation of DC-link voltage oscillations to reduce size of DC-side capacitor and improve lifetime of power converter. *Electr Power Syst Res* 2021;194:107048.
- [30] Afshari E, Moradi GR, Yang Y, Farhangi B, Farhangi S. A review on current reference calculation of three-phase grid-connected PV converters under grid faults. In: 2017 IEEE power and energy conference at Illinois. PECE, IEEE; 2017, p. 1–7.
- [31] Benyamina F, Benrabah A, Khoucha F, Zia MF, Achour Y, Benbouzid M. Online current limiting-based control to improve fault ride-through capability of grid-feeding inverters. *Electr Power Syst Res* 2021;201:107524.
- [32] Afshari E, Moradi GR, Rahimi R, Farhangi B, Yang Y, Blaabjerg F, Farhangi S. Control strategy for three-phase grid-connected PV inverters enabling current limitation under unbalanced faults. *IEEE Trans Ind Electron* 2017;64(11):8908–18.
- [33] Silva RM, Cupertino AF, Rezende GM, Sousa CV, Mendes VF. Power control strategies for grid connected converters applied to full-scale wind energy conversion systems during LVRT operation. *Electr Power Syst Res* 2020;184:106279.
- [34] Safa A, Berkouk EM, Messlem Y, Gouichiche A. A robust control algorithm for a multifunctional grid tied inverter to enhance the power quality of a microgrid under unbalanced conditions. *Int J Electr Power Energy Syst* 2018;100:253–64.
- [35] Zhou L, Liu J, Zhou S. Improved demagnetization control of a doubly-fed induction generator under balanced grid fault. *IEEE Trans Power Electron* 2015;30(12):6695–705. <http://dx.doi.org/10.1109/TPEL.2014.2382603>.
- [36] Xiao X-Y, Yang R-H, Zheng Z-X, Wang Y. Cooperative rotor-side SMES and transient control for improving the LVRT capability of grid-connected DFIG-Based wind farm. *IEEE Trans Appl Supercond* 2019;29(2):1–5. <http://dx.doi.org/10.1109/TASC.2018.2881315>.
- [37] Döşoğlu MK, Güvenç U, Sönmez Y, Yılmaz C. Enhancement of demagnetization control for low-voltage ride-through capability in DFIG-based wind farm. *Electr Eng* 2018;100:491–8.
- [38] Liang J, Qiao W, Harley RG. Feed-forward transient current control for low-voltage ride-through enhancement of DFIG wind turbines. *IEEE Trans Energy Convers* 2010;25(3):836–43. <http://dx.doi.org/10.1109/TEC.2010.2048033>.
- [39] Liang J, Howard DF, Restrepo JA, Harley RG. Feedforward transient compensation control for DFIG wind turbines during both balanced and unbalanced grid disturbances. *IEEE Trans Ind Appl* 2013;49(3):1452–63. <http://dx.doi.org/10.1109/TIA.2013.2253439>.
- [40] Zhu D, Zou X, Dong W, Jiang C, Kang Y. Disturbance feedforward control for type-3 wind turbines to achieve accurate implementation of transient control targets during LVRT. *Int J Electr Power Energy Syst* 2020;119:105954.
- [41] Saeed MA, Khan HM, Ashraf A, Qureshi SA. Analyzing effectiveness of LVRT techniques for DFIG wind turbine system and implementation of hybrid combination with control schemes. *Renew Sustain Energy Rev* 2018;81:2487–501.
- [42] Qin B, Li H, Zhou X, Li J, Liu W. Low-voltage ride-through techniques in DFIG-based wind turbines: A review. *Appl Sci* 2020;10(6):2154.
- [43] Tohidi S, Behnam M-i. A comprehensive review of low voltage ride through of doubly fed induction wind generators. *Renew Sustain Energy Rev* 2016;57:412–9.
- [44] Benbouzid M, Muyeen S, Khoucha F. An up-to-date review of low-voltage ride-through techniques for doubly-fed induction generator-based wind turbines. *Int J Energy Convers* 2015;3(1):1–9.
- [45] Zeb K, Islam SU, Khan I, Uddin W, Ishfaq M, Curi Busarello TD, Muyeen S, Ahmad I, Kim H. Faults and Fault Ride Through strategies for grid-connected photovoltaic system: A comprehensive review. *Renew Sustain Energy Rev* 2022;158:112125.

- [46] Amirat Y, Oubrahim Z, Ahmed H, Benbouzid M, Wang T. Phasor estimation for grid power monitoring: Least square vs. linear Kalman filter. *Energies* 2020;13(10):2456.
- [47] Verma AK, Subramanian C, Jarial RK, Roncero-Sánchez P, Rao UM. A robust Lyapunov's demodulator for tracking of single-/three-phase grid voltage variables. *IEEE Trans Instrum Meas* 2021;70:1–11. <http://dx.doi.org/10.1109/TIM.2020.3043494>.
- [48] Ahmed H, Biricik S, Benbouzid M. Enhanced frequency adaptive demodulation technique for grid-connected converters. *IEEE Trans Ind Electron* 2021;68(11):11053–62.
- [49] Moźdzynski K, Rafał K, Bobrowska-Rafał M. Application of the second order generalized integrator in digital control systems. *Arch Electr Eng* 2014;63(3).
- [50] Biricik S, Komurcugil H, Tuyen ND, Basu M. Protection of sensitive loads using sliding mode controlled three-phase DVR with adaptive notch filter. *IEEE Trans Ind Electron* 2018;66(7):5465–75.
- [51] Chedjara Z, Massoum A, Wira P, Safa A, Gouichiche A. A new quasi open loop synchronization technique for grid-connected applications. *Electr Control Commun Eng* 2021;17(1):47–58.
- [52] Verma AK, Ahmed H, Roncero-Sanchez P, Chaturvedi P. An enhanced single-phase self-tuning filter based open-loop frequency estimator for weak grid. In: *IEEE energy conversion congress and exposition (ECCE)*. IEEE; 2021. <http://dx.doi.org/10.1109/ecce47101.2021.9595504>.
- [53] Ahmed H, Pay ML, Benbouzid M, Amirat Y, Elbouchikhi E. Gain normalized adaptive observer for three-phase system. *Int J Electr Power Energy Syst* 2020;118:105821.
- [54] Ahmed H, Pay ML, Benbouzid M, Amirat Y, Elbouchikhi E. Hybrid estimator-based harmonic robust grid synchronization technique. *Electr Power Syst Res* 2019;177:106013.
- [55] Fortescue CL. Method of symmetrical co-ordinates applied to the solution of polyphase networks. *Trans Am Inst Electr Eng* 1918;37(2):1027–140.
- [56] Kaura V, Blasko V. Operation of a phase locked loop system under distorted utility conditions. *IEEE Trans Ind Appl* 1997;33(1):58–63.
- [57] Lyu S, Zheng L, Song J. A second-order generalized integrator frequency locked loop with damping ratio adaptation. *IEEE Trans Power Electron* 2022;37(3):2694–704.
- [58] Ahmed H, Biricik S, Benbouzid M. Linear Kalman filter-based grid synchronization technique: An alternative implementation. *IEEE Trans Ind Inf* 2020;17(6):3847–56.
- [59] Ahmed H, Benbouzid M. Adaptive observer-based frequency-locked loops for renewable energy systems: A comparative analysis. In: *IECON 2020 the 46th annual conference of the IEEE industrial electronics society*. 2020, p. 4941–6. <http://dx.doi.org/10.1109/IECON43393.2020.9255115>.
- [60] Benyamina F, Benrabah A, Khoucha F, Zia MF, Achour Y, Benbouzid M. An augmented state observer-based sensorless control of grid-connected inverters under grid faults. *Int J Electr Power Energy Syst* 2021;133:107222.
- [61] Teodorescu R, Liserre M, Rodriguez P. Appendix B: Instantaneous power theories. In: *Grid converters for photovoltaic and wind power systems*. John Wiley & Sons, Ltd; 2010, p. 363–79. <http://dx.doi.org/10.1002/9780470667057.app2>.
- [62] Mahamedi B, Eskandari M, Fletcher JE, Zhu J. Sequence-based control strategy with current limiting for the fault ride-through of inverter-interfaced distributed generators. *IEEE Trans Sustain Energy* 2018;11(1):165–74.
- [63] Bhoreddy M, Subramaniam S, Nanjappagounder AG, Isaac A, Natarajan B. Dynamic performance enhancement of grid tied PV system under abnormal grid conditions employing an effective peak current-limiting control strategy. *Int Trans Electr Energy Syst* 2020;e12542.
- [64] Sadeghkhani I, Golshan MEH, Guerrero JM, Mehrizi-Sani A. A current limiting strategy to improve fault ride-through of inverter interfaced autonomous microgrids. *IEEE Trans Smart Grid* 2016;8(5):2138–48.
- [65] Rocabert J, Luna A, Blaabjerg F, Rodriguez P. Control of power converters in AC microgrids. *IEEE Trans Power Electron* 2012;27(11):4734–49.
- [66] Cupertino AF, Xavier LS, Brito EM, Mendes VF, Pereira HA. Benchmarking of power control strategies for photovoltaic systems under unbalanced conditions. *Int J Electr Power Energy Syst* 2019;106:335–45.
- [67] Sadeghkhani I, Golshan MEH, Mehrizi-Sani A, Guerrero JM. Low-voltage ride-through of a droop-based three-phase four-wire grid-connected microgrid. *IET Gener Transm Distrib* 2018;12(8):1906–14.
- [68] Masetti C. Revision of European Standard EN 50160 on power quality: Reasons and solutions. In: *Proceedings of 14th international conference on harmonics and quality of power-ICHQP 2010*. IEEE; 2010, p. 1–7.
- [69] Dai Z, Lin W, Lin H. Estimation of single-phase grid voltage parameters with zero steady-state error. *IEEE Trans Power Electron* 2015;31(5):3867–79.
- [70] Pay ML, Cao P, Sun Y, McCluskey D. Luenberger observer based grid synchronization techniques for smart grid application. In: *IECON 2020 the 46th annual conference of the IEEE industrial electronics society*. IEEE; 2020, p. 4955–60.
- [71] Gulur S, Iyer VM, Bhattacharya S. A dual-loop current control structure with improved disturbance rejection for grid-connected converters. *IEEE Trans Power Electron* 2019;34(10):10233–44. <http://dx.doi.org/10.1109/TPEL.2019.2891686>.